UNIVERSITY OF CALIFORNIA

Santa Barbara

Thermal Conductivity and Anisotropy of Layered Oxides

A thesis submitted in partial satisfaction of the

requirements for the degree Masters of Science

in Materials

by

Taylor David Sparks

Committee in charge:

Professor David R. Clarke

Professor Ram Seshadri

Professor Ted Bennett

March 2010

The thesis of Taylor David Sparks is approved.

_____

Ram Seshadri

_____

Ted Bennett

_____

David R. Clarke, Committee Chair

March 2010

Thermal Conductivity and Anisotropy of Layered Oxides

by

Taylor David Sparks

ACKNOWLEDGEMENTS

I would like to thank the contributions of my fellow researchers Wan Chunlei, Qu Zhixue, Shen Yang, Andi Limarga and the helpful guidance of advisors David Clarke and Pan Wei and committee members Ram Seshadri and Ted Bennett. Most importantly, deep gratitude is extended to my wife, Jodi Sparks, who tolerates my long hours immersed in coursework or in the lab and was even willing to follow me across the country so that I can accomplish my dreams.

This work was supported under the auspices of a National Science Foundation's Materials World Network grant DMR-0710523 on "Discovery of Low Thermal Conductivity Materials" through the University of California, Santa Barbara.

ABSTRACT

Thermal Conductivity and Anisotropy of Layered Oxides

by

Taylor David Sparks

The thermal conductivity of a series of complex layered oxides including $RE_2SrAl_2O_7$, with different rare-earth (RE) ions, and $Sr_2Nb_2O_7$ has been measured up to 1000^{o}C. The temperature dependence and anisotropy are considered. The aluminates exhibit a strong dependence on the atomic number of the RE ion, ranging from an approximately 1/T dependence for RE=La to an almost temperature independent behavior of RE=Dy. A standard phonon-phonon scattering model modified to account for a minimum phonon mean free path was used to fit the thermal conductivity. The difference in behavior is attributed to increased phonon-phonon scattering with the atomic mass of the rare-earth ion. Although a satisfactory parametric fit is obtained, the model does not take into account either the detailed layer structure of the aluminates, consisting of alternating rock-salt and perovskite layers in a natural superlattice structure, or the site preferences of the rare-earth ion. This suggests that further model

development is warranted. The niobates demonstrate anisotropy in thermal properties that persists through an incommensurate-normal ferroelectric phase transformation at 215^{o}C and up to 1000^{o}C, the maximum temperature of our measurements. The thermal conductivity perpendicular to the perovskite layers, derived from the diffusivity in the same direction, calculated using the density and measured heat capacity, has a constant value of 1.05 W/mK up to 1000^{o}C. Possible explanations for the low thermal conductivity and anisotropy are described.

TABLE OF CONTENTS

LIST OF FIGURES

1. Introduction

1.1 Background and Motivation

Layered oxides exhibit unique properties such as high temperature super-conduction in $YBa_2Cu_3O_7$ and $Bi_2Sr_2CaCu_2O_8$ materials[1; 2], good high temperature thermoelectric response in $NaCo_2O_4$ and $Ca_3Co_4O_9$ materials[3; 4] and unique magnetic and electronic properties in $RE_3Mn_2O_7$ (RE =rare-earth cation) materials[5; 6]. The relationship between the crystal structure, or more specifically, the block structure that the layers comprise, and the observed properties have been extensively studied over the past several decades. However, despite the extensive literature[7-10] on the thermal properties of superconductors, the true nature of thermal transport is not fully understood. The goal of this document is to better comprehend the effect of crystal structure on the thermal conductivity through analysis on relevant layered oxide material systems.

A better understanding of the thermal properties of layered oxides is clearly needed and justification for research already exists. For example, low thermal conductivity materials are critically necessary for applications including thermal barrier coatings and thermoelectrics. Additionally, thermal anisotropy is necessary for heat spreading applications like those found in electronic packaging.

The principle reason for this work, however, is to demonstrate adequate understanding and creative application of the theory and fundamentals taught during the graduate level coursework required for the Master's degree. Since the

coursework centered around structural and inorganic materials, crystal structures, crystallography and the quantum theory of solids this research topic provides a satisfactory opportunity to apply what I have learned and demonstrate thorough analysis. Nevertheless, before we can begin to look at the materials selection steps, the crystal structure of the oxides of interest or the findings of the research we must first build a foundation of understanding of the basic theory of thermal conductivity.

1.2 Thermal Conductivity of Oxides

Thermal conductivity is the rate at which heat is transported across a temperature gradient. According to Fourier's Law the relationship between heat flow, *Q*, thermal conductivity, *κ*, and temperature gradient, ∇T, can be expressed generally as

$$Q = -\kappa\,(\nabla T). \tag{1}$$

The heat transported across a temperature gradient must be carried by either delocalized charged particles or by quantized wavepackets of energy manifested as waves of displaced atoms called phonons. The thermal conductivity consists of independent contributions from electrons and phonons as

$$\kappa_{total} = \kappa_e + \kappa_{ph}. \tag{2}$$

The thermal conductivity of insulating oxides differs from that of metals in that the heat is primarily carried via phonon transport, termed lattice thermal conductivity, as opposed to conducting electrons.

Thermal conductivity is a difficult property to measure directly for several reasons. The heat flux is hard to measure exactly, perfect uniaxial heat flow is difficult to achieve because of heat losses in the radial directions, temperature measurement are imperfect and steady-state conditions can take a long time to achieve. Instead, experimental techniques normally measure the thermal diffusivity, α, defined as the rate of temperature change with time. However, the two properties are related by the following

$$\kappa = \rho\, C_p\, \alpha \tag{3}$$

where C_p is the heat capacity at constant pressure and ρ is the density.

The thermal conductivity of non-metallic crystals, including the majority of oxides, exhibits four distinct regimes when plotted against temperature. This is shown in Figure 1. The key to understanding the temperature dependence of thermal conductivity is to realize that the phonons responsible for carrying heat undergo scattering events proportional to the number of scattering sites present including defects and other phonons. According to the Bose-Einstein statistical factor the number of phonons present, n, is

$$n = \frac{1}{exp\,(\hbar\omega/k_B\,T)-1} \approx \frac{k_B\,T}{\hbar\omega}. \tag{4}$$

At low temperatures, in the A regime, there is very little thermal energy to excite phonons. Therefore, the phonon mean-free-path is limited by defects and boundary whose presence is temperature independent. The T^3 temperature dependence of thermal conductivity must then be explained by the heat capacity having a T^3 dependence at very low temperatures.

The B regime, characterized by a maximum in thermal conductivity occurs when the phonon mean-free-path of phonon-phonon collisions is equal to phonon-defect collisions. Although this temperature will certainly vary with defect type and concentration, Grimvall[11] estimates this value to be approximately $0.1\theta_D$.

At temperatures above this peak, in the C regime, the thermal conductivity exhibits a 1/T dependence. This is because anharmonic phonon scattering, due to phonon-phonon interactions dominate. If more phonons are present then the likelihood of scattering should increase. Since equation 4 shows that $n \sim T$ then the phonon mean-free-path, $\Lambda \sim 1/T$ for three-phonon processes and $\sim 1/T^2$ for four-phonon processes. This quantitatively explains the 1/T temperature dependence of the C regime.

Finally, at very high temperatures the D regime tends towards having no temperature dependence. The physical explanation for this is that phonons are waves of displaced atoms and the mean-free-path cannot be decreased smaller than the distance between two neighboring atoms.

The standard treatment of thermal conductivity of solids is based on Debye's extension of the kinetic theory of gases[12]. The phonons responsible for carrying heat can be considered as a gas of massless particles experiencing collisions with other phonons or with lattice imperfections. Based on this analogy to the kinetic theory of gases, there have been two methods derived to calculate thermal conductivity. The first considers the phonon relaxation time and the second considers the phonon mean-free-path. Each will be discussed in turn.

1.2.1 Phonon Relaxation Time Method

Callaway and Baeyer[13] calculate the thermal conductivity by using the phonon relaxation time method. This method integrates over the all possible phonon frequencies as

$$\kappa = \frac{1}{3}\int_0^{\omega_D} \tau \, v_s^2 \, C(\omega) \, d\omega. \tag{5}$$

where τ is the phonon relaxation time, v_s is the velocity of sound, C is the specific heat and ω is the phonon frequency. The phonon relaxation time varies depending on the scattering mechanism involved. For example, for phonon-phonon scattering at high temperatures the relaxation time is expressed as

$$\tau_p^{-1} = C \, T \, \omega^2 \tag{6}$$

where C is a constant, but for point defect scattering the phonon relaxation time is approximated by Rayleigh scattering as

$$\tau_d^{-1} = A \, \omega^4. \tag{7}$$

Rayleigh scattering is normally only applied to situations where the scattering site is much smaller than the incident wavelength, however, it is a valuable approximation of phonon scattering from defects. Additional scattering mechanisms exist such as mass disorder, grain boundaries, etc and could be included but for the sake of simplicity we will simply take the total phonon relaxation time to be:

$$\tau_c^{-1} = \tau_p^{-1} + \tau_d^{-1}. \tag{8}$$

By using the substitution $x = \hbar\omega/k_BT$ the integral in equation 3 becomes

$$\kappa = \frac{k_B}{2\pi^2 v_s}\left(\frac{k_B T}{\hbar}\right)^3 \int_0^{\theta/T} \tau_c(x)\frac{x^4 e^x}{(e^x-1)^2}\,dx. \tag{9}$$

The total phonon relaxation time can be rewritten in terms of x as well

$$\tau_c^{-1} = Dx^4 + Ex^2 \tag{10}$$

with

$$D = A\left(\frac{k_B T}{\hbar}\right)^4 \text{ and } E = C\,T\left(\frac{k_B T}{\hbar}\right)^2 \tag{11}$$

at high temperatures. Equation 7 becomes

$$\kappa = \frac{k_B}{2\pi^2 v_s}\left(\frac{k_B T}{\hbar}\right)^3 \int_0^{\theta/T} \frac{x^2}{Dx^2+E}\frac{e^x}{(e^x-1)^2}\,dx. \tag{12}$$

Integrating we obtain in terms of constants D and E

$$\kappa = \frac{k_B}{2\pi^2 v_s (D\,E)^{1/2}}\left(\frac{k_B T}{\hbar}\right)^3 \tan^{-1}\left[\frac{\theta_D}{T}\left(\frac{D}{E}\right)^{1/2}\right] \tag{13}$$

or, using the constants *A* and *C* instead we obtain

$$\kappa = \frac{k_B}{2\pi^2 v_s (A\,C\,T)^{1/2}}\tan^{-1}\left[\frac{k_B\theta_D}{\hbar}\left(\frac{A}{C\,T}\right)^{1/2}\right]. \tag{14}$$

If the material is pure then the term accounting for strong defect scattering, τ_d^{-1}, will be negligible compared to the term for phonon-phonon scattering, τ_p^{-1}, resulting in

$$\kappa = \frac{{k_B}^2}{2\pi^2 \hbar v_s} \frac{\theta_D}{C\,T}. \tag{15}$$

Alternatively, in the limit of strong defect scattering the τ_d^{-1} term dominates and the following thermal conductivity expression is obtained:

$$\kappa = \frac{k_B}{4\pi\, v_s} \frac{1}{(A\,C\,T)^{1/2}}. \tag{16}$$

1.2.2 Phonon Mean-Free-Path Method

Roufosse and Klemens[14] developed a very similar treatment of thermal conductivity based on the changing mean-free-path rather than the phonon relaxation time. While similar, the derivation is worth following, because it serves as the basis for the introduction of an important concept, that of the minimum phonon mean-free-path. The derivation begins with the standard equation

$$\kappa = \frac{1}{3}\int_0^{\omega_D} \mathrm{C}(\omega, \mathrm{T})\, \mathrm{v_s}\, \Lambda(\omega, \mathrm{T})\, \mathrm{d}\omega. \tag{17}$$

At temperatures greater than the Debye temperature *C(ω)* is proportional to ω^2:

$$C = B\,\omega^2 \tag{18}$$

where *B* is a constant. Similar to phonon relaxation times, the total phonon mean-free-path actually consists of contributions from Umklapp phonon-phonon interactions as well as phonon-defect interactions

$$\Lambda_c^{-1} = \Lambda_{ph}^{-1} + \Lambda_d^{-1} = \frac{\omega^2 T}{D_{ph}} + \frac{c_d \omega^4}{D_d} \quad (19)$$

where c_d is the concentration of defects, and D_{ph} and D_d are constants. For pure materials equation 17 becomes

$$\kappa = \frac{1}{3}\int_0^{\omega_D} \mathrm{B}\,\omega^2\,\mathrm{v_s}\,\frac{\mathrm{D_{ph}}}{\omega^2\,\mathrm{T}}\,\mathrm{d}\omega = \frac{\mathrm{B\,v_s\,D_{ph}\,\omega_D}}{3\,\mathrm{T}} = \frac{A}{T}. \quad (20)$$

where the parameter *A* can be expressed in terms of atomistic and crystal structure properties:

$$A = \frac{B'}{(2\pi)^3}\,\bar{M}\,\bar{\Omega}^{1/3}\,\frac{k_B^3\,\Theta_D^3}{\hbar^3\gamma^2} \quad (21)$$

$\overline{M}$ is the average atomic mass of the atoms in the unit cell, $\bar{\Omega}$ is the average atomic volume (the volume of the unit cell divided by the number of atoms in the unit cell), γ is the Grunisen constant, Θ_D is the Debye temperature and *B'* is a constant. The other constants are the Boltzmann and Planck's constants. In turn, the Debye temperature can be expressed in terms of the acoustic velocity, *v*, and the mean atomic size, $\bar{\Omega}^{1/3}$.

$$\Theta_D = \frac{v\,\hbar}{k_B}\left(\frac{6\pi^2}{\bar{\Omega}}\right)^{1/3} \quad (22)$$

If the acoustic velocity is taken to be the mean wave velocity[12], v_m,

$$v_m = 3^{1/3}\left(\frac{1}{v_p^3} + \frac{2}{v_S^3}\right)^{-1/3} \quad (22)$$

then to a very good approximation, this can be written in terms of the Young's modulus, E, and the density, expressed in terms of the mean atomic mass and the mean atomic volume:

$$v_m = 0.87\sqrt{\frac{E}{\rho}} = 0.87\sqrt{\frac{E\,\bar{\Omega}}{\bar{M}}} \tag{23}$$

Taken together, the thermal conductivity can be written as:

$$\kappa = \frac{E^{3/2}\;\bar{\Omega}^{5/6}}{\gamma^2\,\bar{M}^{1/2}}\;\frac{B}{T} \tag{24}$$

where *B* is a new constant: $B = B'\,\frac{3}{4\pi}\,(0.87)^3$ and meaning that *A* can be expressed as:

$$A = B\;\frac{E^{3/2}\;\bar{\Omega}^{5/6}}{\gamma^2\,\bar{M}^{1/2}} \tag{25}$$

At high temperatures, above the Debye temperature, the phonon frequency distribution increases with temperature and the mean-free-path approaches the minimum possible in a crystalline solid, namely the inter-atomic spacing. This modifies the temperature dependence of the anharmonic phonon scattering from the 1/T dependence expressed in equation 24. To account for the minimum phonon mean-free-path, Mevrel and colleagues[15] have suggested that the thermal conductivity can then be written in the form:

$$\kappa = \frac{A}{T}\left[\frac{2}{3}\sqrt{\frac{T_1}{T}} + \frac{T}{3\,T_1}\right] = \frac{2\,A\sqrt{T_1}}{T^{3/2}} + \frac{A}{3\,T_1} \tag{26}$$

Where the second term, $A/3T_1$, is the limiting value of the thermal conductivity at high temperatures, also referred to as κ_{min}, when the phonon mean-free-path is the same as the inter-atomic spacing.

Having completed this introduction to thermal conductivity calculations we now continue to the focus of this document, thermal conductivity of layered oxides, including the successful modeling of thermal conductivity.

1.3.1 Materials Selection Guidelines

Guidelines for identifying superior candidates for low thermal conductivity materials have been previously identified[16]. Materials with large, complex unit cells, high average atomic mass, high average atomic volume and finally structural, mass and bonding disorder should exhibit low thermal conductivity. Materials likely to have anisotropic thermal properties should have an anisotropic crystal structure or superlattice. Synthetic superlattices such as W/Al_2O_3 nanocomposites[17] and WSe_2 disordered films[18] have been reported to have ultra low thermal conductivity. Naturally occurring crystal structures with superlattices of layered perovskites are also common with the added benefit of high temperature stability and facile synthesis; examples include $CsCa_2Nb_3O_{10}$ with the Dion-Jacobsen structure[19-21], $Bi_4Ti_3O_{12}$ with the Aurivillius structure[22; 23], and $A_{n+1}B_nO_{3n+1}$ A = (RE, Sr) B = (Ti, Al) with the Ruddlesden-Popper structure[24; 25].

The present work considers the $RE_2SrAl_2O_7$ (RE = La, Nd, Sm, Eu, Gd, Dy) compound[26] as well as La doped $Sr_2Nb_2O_7$ compound[27]. These material systems are natural superlattices and they coincide with the above identified guidelines for low thermal conductivity. A phase transition present in strontium niobate allowed the

effect of atomic displacement and octahedral tilting and rotation on thermal conductivity to be observed. Additionally, in the rare-earth strontium aluminate system, the effect of cation ordering, mean atomic mass and volume on the thermal properties was observed by altering the choice of the rare-earth cation. The comparison of thermal properties to existing models will then be considered. A correct understanding of the crystal structure of these compounds would be instructive prior to any analysis. For this reason, the crystal structure of these systems will be described in subsequent sections.

Single crystals are normally utilized to determine the principle coefficients of the thermal conductivity tensor as well as its anisotropy. However; in the absence of large single crystals, highly textured samples (where the grains have been preferentially oriented) and polycrystalline samples can be used together in an alternate approach based on the symmetry considerations of the thermal diffusivity tensor to determine the anisotropy of the thermal conductivity.

1.4.1 Crystal Structure of $RE_2SrAl_2O_7$

Rare-earth strontium aluminate crystallizes in the n=2 member of the Ruddlesden-Popper structure, a perovskite derivative. The crystal structure is tetragonal in the space group I4/mmm. The lattice parameters vary slightly with the choice of rare-earth cation, these values are recorded in Table 1. The structure can be envisioned as a double-perovskite layer separated by a rock salt layer. The

perovskite block consists of vertex-shared AlO_6 octahedra which exhibit no significant tilting or rotations. The Sr^{2+} and RE^{3+} cations are distributed between two crystallographically distinct cation sites termed A1 and A2. The A1 site, hosting 1/3 of the cations, is 12 coordinate and lies within the double perovskite block. The A2 site, hosting 2/3 of the cations, is 9 coordinate and lies within the rocksalt block. The crystal structure is shown in Figure 2 with the different sites and block layers indicated.

Zvereva et al.[28] carried out structural characterizations on the entire series of $RE_2SrAl_2O_7$ (RE = La, Nd, Sm-Ho). Exact atomic positions, lattice parameters and inter-atomic distances were determined using Rietveld refinement. Moreover, an important finding from Zvereva et al.'s study was the tendency of cation ordering as the rare-earth cation is varied across the lanthanide series. As the RE^{3+} cation is varied from La^{3+} to Ho^{3+} there is a systematic variation in cation site occupancy; the RE^{3+} cation sits increasingly on the A2 site while the Sr^{2+} cation sits increasingly on the A1 perovskite site. The ordering is driven by energy minimization. The lanthanide contraction dictates that the RE^{3+} cations decrease in ionic radius going across the series. In order to minimize strain, these smaller cations are more likely to sit on the smaller 9 coordinate site, A2, within the rocksalt block rather than in the larger 12 coordinate site, A1, within the perovskite block. The site occupancy and lattice parameters for the series are shown in Table 1.

1.4.2 Crystal Structure of La doped $Sr_2Nb_2O_7$

The orthorhombic crystal structure of $Sr_2Nb_2O_7$, shown in Figure 3, is also a derivative of the perovskite structure. Unlike the Ruddlesden-Popper structure, the strontium niobate structure has perovskite slabs consisting of vertex-shared NbO_6 octahedra are separated by additional O atoms[29-32] instead of rocksalt blocks. The perovskite layers are offset by shear of a/2 with respect to one another. The $Sr_2Nb_2O_7$ compound is part of a homologous series having the chemical composition $Sr_nNb_nO_{3n+2}$[33] where n denotes the number of NbO_6 octahedra comprising the perovskite slab thickness. Only n=4 and n=5 members of the series have been observed so far[34; 33].

Cooling from above the Curie temperature, 1342°C[35], $Sr_2Nb_2O_7$ undergoes a ferroelectric phase transition from space group *Cmcm* to *$Cmc2_1$*, which is commonly referred to as the normal phase, and on further cooling at 215°C[36; 37] the compound transitions to an incommensurate (IC) phase with space group *$Cmc2_1$*.

Due to the anisotropic layered structure the thermal properties should be nearly uniaxial along the b-axis defined to be perpendicular to the layers. However, since $Sr_2Nb_2O_7$ is intrinsically p-type, the electronic contribution to thermal conductivity would mask the true anisotropic nature of the thermal conductivity. For this reason the material was doped with a small amount (0.5 mol %) of La^{3+} cations substituting the Sr^{2+} cations. The new formula can be expressed as $La_{0.005}Sr_{1.995}Nb_2O_7$.

2. Experimental Details

2.1.1 $RE_2SrAl_2O_7$ Sample Preparation

Following the method described by Zvereva et al.[28], four of the aluminates, with RE=Sm, Eu, Gd and Dy, were prepared from stoichiometric mixtures of the oxides (Sigma Aldrich, purity ≥ 99.95%) with $SrCO_3$ (Alfa Aesar, purity ≥ 99.99%) powder, which were calcined at 1100^{o}C for 8 hours, ground and then sintered at 1550^{o}C for 5 hours in air. Prior to mixing, the rare-earth oxides were heated for 8 hours at 1000^{o}C to remove any adsorbed CO_2 and H_2O. The other two aluminates, $La_2SrAl_2O_7$ and $Nd_2SrAl_2O_7$, were prepared by a co-precipitation method from nitrate solutions. Nitrate solutions were prepared from Sr_2NO_3 (Sigma Aldrich, purity ≥ 99.99%) and $Al(NO_3)_3$ (Sigma Aldrich, purity ≥ 99.9) and La_2O_3 or Nd_2O_3 (Sigma Aldrich, purity ≥ 99.95%) powders dissolved in excess nitric acid. The mixed nitrate solutions were slowly added into ammonia to produce gel-like precipitates that were washed and filtered and then washed in ethyl alcohol. The washed precipitates were dried overnight at 120^{o}C and then calcined at 900^{o}C for five hours before grinding, sieving in a 325 mesh, cold-pressing at 200 MPa and sintering in air at 1550^{o}C for five hours.

2.1.2 La doped $Sr_2Nb_2O_7$ Sample Preparation

Two different techniques were used to create randomly oriented polycrystalline samples and highly crystallographically textured samples. The former

samples were prepared by conventional sintering and the latter were prepared by hot-forging. Sintered samples were made by the co-precipitation method described by Brahmaroutu et al.[38] Starting materials were NbC_2O_4 (Alfa Aesar, purity ≥ 99.99%), La_2O_3 (Alfa Aesar, purity ≥ 99.99%) and Sr_2NO_3(Sigma Aldrich, purity ≥ 99.99%). Stoichiometric quantities of NbC_2O_4 dissolved in excess oxalic acid, La_2O_3 dissolved in excess nitric acid, and Sr_2NO_3 dissolved in de-ionized water were mixed. The resultant solution was coprecipitated by adding it drop by drop to excess NaOH solution maintained at a constant pH of 12 with vigorous stirring. The gel-like precipitants were filtered using a centrifuge, washed twice in de-ionized water and twice in ethanol. The washed precipitates were dried overnight at 110^{o}C and calcined at 1000^{o}C for 2 hours. The calcined powders were then sieved in a 325 mesh, pressed into pellets at 200 MPa and sintered at 1400^{o}C for 2 hours.

The textured samples were prepared by the hot forging method described by Fuierer and Newnham[39]. Starting materials were SrO (Sigma Aldrich, purity ≥ 99.99%), La_2O_3 (Alfa Aesar, purity ≥ 99.99%), and Nb_2O_5 (Alfa Aesar, purity ≥ 99.99%). The oxide powders were pre-calcined to 1000^{o}C for 2 hours to remove hydroxide and adsorbed CO_2 and H_2O. Powders were weighed and stoichiometric quantities were mixed together and ball milled in ethanol overnight with zirconia media. The mixture was dried and then calcined at 900^{o}C for 2 hours. The powders were sieved in a 325 mesh, pelletized and then hot forged.

2.2 Characterization

Phase identification and analysis was performed by X-ray diffraction (XRD) using an X-ray diffractometer (Phillips, X'Pert Pro, Holland) with nickel-filtered Cu Kα radiation. The density, ρ, of the samples was measured by the Archimedes method with de-ionized water as the immersion medium. The heat capacity, C_p, was measured using a differential scanning calorimeter (DSC, Netzsch, Pegasus 404C, Germany) in an Argon gas atmosphere from 35 to 1100^{o}C. The values were determined according to the ASTM standard E1269-95. Elastic constant measurements were made by sonic velocity measurements.

The thermal diffusivity, α, was measured using an Anter Flashline 3000 thermal flash system (Pittsburgh, PA) with a high-speed xenon flash lamp. The samples for the thermal diffusivity measurements were machined to be coplanar with a thickness of approximately 1 mm and a diameter of 12.5 mm. Prior to the measurements, both sides of each sample were coated with thin layers of Ti and Pt using electron beam physical vapor deposition to minimize the possibility of radiative transport through the translucent samples. The Ti adhesion layer was approximately 10 nm thick while the Pt layer was about 750 nm. The samples were then spray coated with colloidal graphite on both sides to ensure full absorption and maximum optical absorption and emissivity. Thermal diffusivity was measured in an Argon gas atmosphere from 35 to 1000^{o}C at intervals of 100^{o}C with a comparison measurement at 100^{o}C when cooling down to ensure reproducibility of

the measurements and to identify if the coatings remained intact. The thermal diffusivity values were determined using the Clarke and Taylor model[40]. At temperatures above ~700^{o}C there was a very small instantaneous detection on the backside of the sample indicative of radiative transport. Correction of the high-temperature diffusivity measurements for radiative heat transfer through the samples was performed using a numerical method[41] that removes the initial instantaneous detection peak.

3. Results

3.1 X-ray Diffraction

All six of the aluminate compounds synthesized were phase pure as assessed by X-ray diffraction and exhibited the peak height distributions expected for random, polycrystalline material. As shown in Figure 4 the peak positions and heights vary systematically as the rare-earth ion is altered. Similarly, the The X-ray results for $Sr_2Nb_2O_7$, shown in Figure 5, indicate that both the sintered and hot-forged samples were single phase. All the peaks correspond to the orthorhombic phase. The hot forged sample exhibited very strong (0k0) peaks. The other peaks found in random samples and listed in the JCPDS file are absent[42]. This indicates that the hot forged samples were strongly textured along the crystallographic *b*-axis. The degree of orientation was quantified by calculating the Lotgering factor *f*

from the x-ray peak intensities[43]. For the hot-forged samples the maximum out of plane orientation was found to be > 95%.

3.2 Density

The availability of fully dense, pore free ceramics is critical to obtaining reliable thermal diffusivity measurements. With the exception of the $La_2SrAl_2O_7$ compound, all the aluminates densified to greater than 95% of their theoretical values. Similarly, the strontium niobate, both the textured sinter forged sample as wells as the polycrystalline sample were densified to greater than 97% of the theoretical value (Table 2).

3.3 Heat Capacity

The temperature dependence of the heat capacity of the rare-earth strontium aluminate and the strontium niobate compounds are shown in Figures 5 and 6 respectively. The heat capacity of the rare-earth strontium aluminates increase monotonically with temperature throughout the entire temperature range. The strontium niobate compounds follow a similar trend except close to the second order phase transition of the normal phase at ≈215^{o}C indicated by the small exothermic peak. The heat capacity data for both series was compared by also calculating the heat capacity according to the Neumann-Kopp rule from the chemical compositions and the literature data of its constituent oxides[44]. The

calculated values for heat capacity were within ± 4.2% of the measured values. This variation is consistent with other studies.

3.4 Thermal Diffusivity

The thermal diffusivity measurements of both series are shown in Figure 8 and 9. The rare-earth strontium aluminates decrease monotonically with temperature. The diffusivity values generally decrease with increasing mass of the rare-earth cation. The variation in temperature dependence will be discussed with the thermal conductivity results.

In the strontium niobate compounds there are two regimes discernable, one below and one above the temperature of the phase transition from the normal phase to the incommensurate phase. The lower temperature regime is more strongly temperature dependent with a slope ranging from -1.8×10^{-6} to -4.8×10^{-6} $cm^2\ s^{-1}\ K^{-1}$. Above the phase transition temperature, the diffusivity of the textured sample was constant with temperature whereas that of the randomly oriented polycrystalline sample decreased slightly.

4. Discussion

4.1.1 Thermal Conductivity of $RE_2SrAl_2O_7$

The thermal conductivities were calculated from the measured diffusivities, α_{ij}, densities, ρ, and specific heat values, C_p, using equation 3. The values

determined in this way for the rare-earth strontium aluminates are plotted in Figure 10.

There are two striking features of the thermal conductivity data shown in Figure 10. The first is the remarkable difference in the thermal conductivity with temperature of the different rare-earth strontium aluminates. Furthermore, since the difference in the ionic size and ionic mass between the rare-earth ions in the aluminates studied is relatively small, it is surprising that this can account for the observed temperature dependence. The second is the unusually low thermal conductivity of all the aluminates in approaching the high temperature limit, where the conductivity is independent of temperature. These observations will be explained in turn.

To place the conductivities in context, the thermal conductivities of undoped monoclinic zirconia and yttria-stabilized zirconia[15] (YSZ) are included in Figure 11. From the comparison, the behavior of the lanthanum strontium aluminate is similar to that of undoped zirconia whereas that of the dysprosium strontium aluminate is similar in character to that of yttria-stabilized zirconia. The other aluminates lie in between these two contrasting behaviors. The comparisons are illuminating because the marked temperature dependence of undoped zirconia is characteristic of the ~ 1/T dependence attributed to anharmonic phonon scattering observed in oxides that do not contain high concentrations of point defects or other scattering centers. Similar behavior is also reported for the

majority of oxides. The oxides that typically exhibit little or no temperature dependence are either amorphous, such as silica, or contain very high concentrations of point defects. The latter is exemplified by yttria-stabilized zirconia which typically contains several percent of oxygen vacancies introduced to charge compensate for the alio-valent stabilizing yttrium ion (Y^{3+}). In the case of amorphous materials, the minimum phonon mean-free-path is limited by the size of the structural unit making up the amorphous structure. In both classes of material, the thermal conductivity is limited as the mean-free-path approaches atomic dimensions even at temperatures as low as room temperature[45-48]. None of the rare-earth strontium aluminates contain oxygen vacancies or any other structural defects, so the contrasting behavior of the different aluminates must have a different origin.

Mass disorder has been observed as a phonon scattering mechanism in systems such as Si-Ge and $(Zr_{1-x}Hf_x)_{1-y}Y_yO_{2-y/2}$[49; 50]. Mass disorder is possible in the $RE_2SrAl_2O_7$ compounds because RE^{3+} is approximately twice as heavy as Sr^{2+} and both share A1 & A2 sites. However, this is not likely because the compound with the greatest disorder, $La_2SrAl_2O_7$, with near equal occupancy of both ions on both sites, has the highest thermal conductivity. Meanwhile, the most ordered compound, $Dy_2SrAl_2O_7$, has the lowest thermal conductivity.

Using the exact atomic positions as wells as the cation site occupancy details from Zvereva's report we were able to calculate the density of the rocksalt and

double perovskite blocks. The much heavier rare-earth cations sit increasingly in the rocksalt layer increasing the in density of the rocksalt layer relative the double perovskite layer. The ratio of the two densities systematically increases across the series from approximately equal, 0.938, in the $La_2SrAl_2O_7$ case to 1.46 in the $Dy_2SrAl_2O_7$ case. The complete set of density ratios is tabulated in Table 1. The possible effect on thermal conductivity due to such large differences in block density will be discussed later.

4.1.2 Thermal Conductivity of La doped $Sr_2Nb_2O_7$

The thermal conductivity and anisotropy in the strontium niobate samples were determined by a tensorial analysis approach[51] explained below. The diffusivity measurements in Figure 9 clearly show that the diffusivity perpendicular to the perovskite layers is substantially smaller than that of the randomly oriented polycrystalline material. Furthermore, similar to what was observed with the rare-earth strontium aluminates, the diffusivity is unusually small and temperature independent up to the maximum temperature measured. Although samples textured with the perovskite layers parallel to the heat propagation direction are not available, the well defined crystallography of the two polycrystalline materials enables the diffusivity parallel to the perovskite layers to be calculated using tensorial analysis from the results from the hot-forged and sintered materials as follows.

For an orthorhombic structure, the thermal diffusivity tensor, a second-rank tensor, can be expressed in terms of the diffusivity along the principal crystallographic axes as:

$$\alpha_{ij} = \begin{pmatrix} \alpha_{aa} & 0 & 0 \\ 0 & \alpha_{bb} & 0 \\ 0 & 0 & \alpha_{cc} \end{pmatrix} \quad (27)$$

where the subscripts refer to the crystallographic directions in the unit cell. Although the unit cell of the $Sr_2Nb_2O_7$ structure is strictly orthorhombic, the lattice parameters and sound velocities along the *a*- and *c*-axes are very similar so we can assume that the thermal properties along the *a*- and *c*-axes will also be similar and the diffusivity tensor can be represented by a uniaxial tetragonal tensor:

$$\alpha_{ij} = \begin{pmatrix} \alpha_{aa} & 0 & 0 \\ 0 & \alpha_{bb} & 0 \\ 0 & 0 & \alpha_{cc} \end{pmatrix} = \begin{pmatrix} \alpha_{aa} & 0 & 0 \\ 0 & \alpha_{bb} & 0 \\ 0 & 0 & \alpha_{aa} \end{pmatrix}. \quad (28)$$

The *a* and *c* lattice parameters are reported to be 0.3933 and 0.5683 nm, respectively, whereas the *b* lattice parameter is 2.6726 nm. The sound velocities, v, along the *a*-, b-, and *c*-axes have been measured by Brillioun scattering and are reported to be 4438 ± 25 , 5192 ± 12 and 4458 ± 19 m s^{-1} , respectively[52].

For randomly oriented polycrystalline material, the thermal diffusivity, α_p, can be expressed in terms of the trace of the tensor, namely as:

$$\alpha_p = {}^1/_3\,(2\alpha_{aa} + \alpha_{bb}). \quad (29)$$

Rearranging equation 29, the thermal diffusivity within the *a-c* plane, α_{aa}, can be calculated from the measured diffusivities of the polycrystalline material and the textured hot-forged samples:

$$\alpha_{aa} = {}^{1}/_{2}\left(3\alpha_{p} - \alpha_{bb}\right). \tag{30}$$

The calculated values for the diffusivity parallel to the perovskite planes are shown in the graph of Figure 9 by the circular symbols. Comparison with the other data indicates that the diffusivity is significantly higher, by almost a factor of two, parallel to the planes than perpendicular to the perovskite planes.

An interesting feature of the diffusivity measurements is that the anisotropy is much larger than the anisotropy in either the lattice parameters or the sound velocities. The former is 50% larger in the *b*- direction than in the other directions whereas the sound velocity is only 16% larger. We will return to this point later.

The thermal conductivity is also a second rank tensor and can be computed from the diffusivity using equation 3 substituting α_{ij} for α. Using this relationship as a definition, the conductivities parallel and perpendicular to the perovskite layers can be computed and are shown in Figure 12. The validity of this relationship for aligned anisotropic crystals with blocks of different density can be questioned but is valid for the randomly oriented polycrystalline material.

The temperature dependence of the thermal conductivity of the La-doped $Sr_2Nb_2O_7$ shown in Figure 12 is notable in three respects. Firstly, similar to the rare-earth strontium aluminates, the thermal conductivity is very low and is temperature

independent in contrast to that usually found for defect-free oxides. Secondly, the thermal conductivity does not change, within experimental uncertainty, in crossing the phase transition at 215^{o}C. Thirdly, the thermal diffusivity and conductivity are strongly anisotropic over the entire temperature range measured, up to 1000^{o}C. These features will be discussed in turn.

The low, temperature independent thermal conductivity can be explained by strontium niobate having a very small phonon mean-free-path. The phonon-mean-free path can be calculated from the minimum thermal conductivity which we take as the minimum for the randomly-oriented polycrystalline material, κ_{pm}, estimated from the high temperature limit of the Debye equation,

$$\kappa_{pm} = \frac{C_V v_m \Lambda}{3} \tag{31}$$

where C_V is specific heat at constant volume, v_m is the average phonon velocity and Λ is the phonon mean-free-path. At high temperatures the specific heat per atom, C_V, approaches a value of 3 k_BT according to the Dulong-Petit equation[12] so the minimum thermal conductivity becomes

$$\kappa_{pm} = k_B v_m \bar{\Omega}^{-1} \Lambda. \tag{32}$$

Inverting this equation, the phonon mean-free-path can be calculated from the conductivity of the randomly-oriented material. Using values for the velocity of sound[52], v, of ~4900 m s^{-1} and the average atomic volume, $\bar{\Omega}$, of $Sr_2Nb_2O_7$ of 0.0137 nm^3, the phonon mean-free-path, Λ, is estimated to be 0.301 nm. The mean inter-

atomic spacing, 0.296 nm, was obtained by taking the cube root of the mean atomic volume. This result is consistent with the temperature independence of the thermal conductivity which suggests that the phonon mean-free-path is comparable with the inter-atomic spacings in the structure. If the conductivity perpendicular to the perovskite layers is used in the estimate, the calculated phonon mean-free-path is 0.2 nm.

An alternative explanation for the temperature independence of the conductivity is that the La^{3+} dopant ions act as strong defect scatterers and are responsible for decreasing the thermal conductivity from the temperature dependence given by the Mevrel equation above to the value given by κ_{pm}. The average spacing between dopant ions, randomly distributed within a volume of material, varies with concentration, c, as $c^{-1/3}$. The La^{3+} dopant concentration in the material we have studied is 0.5 mol%. Assuming that they are randomly distributed throughout, the average spacing between La^{3+} ions is 2.47 nm. This is an order of magnitude larger than the inter-atomic distance and hence it is unlikely that this alone could account for enough ionic disorder or structural defects to lower the phonon mean-free-path so significantly. For comparison, this average distance between the La^{3+} ions is substantially larger than the oxygen vacancy spacing which is ~ 0.76 nm in 8YSZ[53]. Similarly, it is unlikely that site disorder of the Sr^{2+} and Nb^{5+} is possible in the crystal structure of the niobate given their different

ionic sizes and site coordination preferences and could contribute to further lowering of the conductivity.

At first sight, the insensitivity of the thermal conductivity to the phase transition as the material transforms from the incommensurate to normal ferroelectric orthorhombic phase is perhaps surprising. However, there appear to be two effects involved associated with the differing temperature dependence of the diffusivity and the specific heat. As indicated by the data in Figure 9 there is a slight change in temperature dependence as the material transforms from the incommensurate to normal orthorhombic phase at 215^{o}C, although the change is small. This is also in the temperature range where the specific heat varies strongly with temperature but with a decreasing slope so the effect on the calculated conductivity is suppressed. In addition, the sound velocity decreases with increasing temperature over the same temperature range further suppressing any change in thermal conductivity in crossing the phase transformation[12]. The second is more fundamental and related to the sampling of the crystal structure by the dominant phonons. As the temperature is raised, the mean energy of the phonons increases and their mean-free-paths decreases and, as indicated in the previous paragraph, they become commensurate with the inter-atomic spacing and hence are insensitive to larger scale structure. It should be noted that a similar insensitivity to a structural rearrangement at a ferroelectric transition has been reported[23] for the

Aurivillius structure compound, $Bi_4Ti_3O_{12}$, which is also a layered ferroelectric oxide and has a ferroelectric transition temperature of 675^{o}C.

The lack of any abrupt change in the conductivity at the phase transformation temperature is further surprising since there are large incommensurate modulations of the structure below the transition temperature. These result in rotational oscillations of the NbO_6 octahedra and large time-dependent displacements of the Sr ions. These are presumably responsible in part for the increase in heat capacity as the transition temperature (insert to Figure 7) is approached from lower temperatures. Finally, similar insensitivity to a structural rearrangement has been reported for the layered ferroelectric oxide $Bi_4Ti_3O_{12}$ which has the Aurivillius structure and a ferroelectric transition temperature of 675^{o}C.

The thermal diffusivity anisotropy and its persistence to high temperatures suggests that it is a consequence of the natural superlattice of repeating $(SrO_2)^{2-}$ and $(Sr_3Nb_5O_{12})^{2+}$ blocks that comprise the layered structure of the strontium niobate. Interestingly, the anisotropy persists to high temperatures where phonons have increased energy that one might think would allow phonons to hop over the $(SrO_2)^{2-}$ block. As will be detailed in the following section, we have been unable to calculate the anisotropy based on existing models in the literature but we note that there is substantial mass difference between the blocks in the structure which would result in significant phonon mismatch. In the normal phase the density of

the $(SrO_2)^{2-}$ block is 3733 kg m^{-3} and the thickness is 0.236 nm whereas the perovskite $(Sr_3Nb_5O_{12})^{2+}$ block has a density of 5527 kg m^{-3} and a thickness of 1.102 nm. The ratio of the density of the different blocks is rather large (1.481:1) resulting in significant acoustic mismatch.

4.2 Thermal Conductivity Modeling

The lattice thermal conductivity of pure, electrically-insulating, defect-free crystalline solids has been studied theoretically in considerable detail based on phonon scattering models. These derivations were included in the introduction.

In comparing our experimental data to equation 26, Mevrel's equation for thermal conductivity accounting for a minimum scattering length, the parameters *A* and T_1 can be used as fitting parameters. The best regression fits to the data for the thermal conductivity of the aluminates is shown by the lines through the data in Figure 10 and the values for the fitting parameters are listed in Table 3. The R^2 values are reasonable given the relatively small number of data points, indicating a good fit to the conductivity data, except for the Gd data. The form of the equation 25 for the parameter A suggests that there is a $M^{-1/2}$ dependence. Strong evidence of this $M^{-1/2}$ dependence is shown by the linear fit (R^2 = 0.97) shown in Figure 13.

As evidenced by the quality of the fits to the data for the different rare-earth aluminates, the anharmonic phonon scattering model including the phonon

wavelength cut-off proposed by Mevrel et al. is excellent in fitting both the temperature and mass dependence of the thermal conductivity. However, it should be emphasized that while the rank ordering of the aluminates is captured through the value of the parameter *A*, the model does not predict the absolute values of the thermal conductivity. In the model, the absolute value depends on the value of *B'*. It has been suggested that the value of *B'* is approximately unity, 1.61 according to Klemens[54]. However, by the fitting of our data to equation 24, the value of *B'* is not a constant and depends on the rare-earth ion. Furthermore, functionally, it appears to have a dependence on the atomic mass. This suggests that there exists a phenomenon that is systematically affecting thermal conductivity that is not included in Mevrel's, or any other model.

Finally, in many respects the finding that the temperature dependence of the thermal conductivity of the series of rare-earth strontium aluminates is consistent with existing models of anharmonic phonon scattering is surprising. The model assumes that the material is homogeneous and isotropic yet the crystal structure is crystallographically anisotropic and consists of alternating layers of perovskite and rock-salt blocks as shown in Figure 2. At very high temperatures, where the phonon scattering length approaches the spacing between atoms, it is reasonable to expect that the detailed atomic arrangement may not affect the phonon scattering but over the temperature range investigated the phonon scattering lengths are larger than this minimum value and so the structure should

not appear to be homogeneous to the phonons. The other feature of these aluminates not incorporated within the phonon scattering model is that the distribution of the rare-earth ions within the rock-salt and perovskite blocks varies with the atomic number. This results in the relative densities of the two blocks changing with increasing atomic number. No phonon scattering model that we are aware of takes into account these detailed crystallographic features or the layered structure of the unit cell of materials such as these aluminates and niobates.

It is concluded that the thermal conductivity and its temperature dependence are determined by a combination of inter-block mass scattering and standard anharmonic phonon scattering. In the aluminates, the inter-block mass scattering is caused by the increasing site preference of the rare-earth ion for the rocksalt block with increasing atomic number of the rare-earth from La^{3+} to Dy^{3+}. The inter-block mass scattering provides a qualitative explanation for the variation from the 1/T type dependence exhibited by the lanthanum strontium aluminate to the temperature-independent behavior of the dysprosium strontium aluminate. The niobates only had 1 composition so the effect of mass or ordering on thermal conductivity wasn't studied as it was with the aluminates.

5. Future Work

The beauty of working with layered oxides is the vast number of compounds available for study. Even minor alterations in composition, cation and anion

substitution, crystal structure, polyhedral rotation and tilting can alter material properties significantly. In addition to the already discussed guidelines for choosing materials with low thermal conductivity we can deduce, based on the findings of this study, a new parameter that should be considered as well, namely, the relative block layer density.

As was pointed out, in both materials studied the thermal conductivity may have been affected by phonon scattering due to a large difference in mass from one block to another. When the ratio of block density was equal, as in the case of $La_2SrAl_2O_7$, there was no abnormal thermal conductivity, yet when the ratio reached 1:146, as in $Dy_2SrAl_2O_7$, or 1:148 in $Sr_2Nb_2O_7$, or 1:2.18 in $Bi_4Ti_3O_{12}$ there was additional scattering resulting in temperature independent thermal conductivity characteristic of highly defected materials. Future studies could look at candidate materials that combine a large ratio of block density with traditional indicators of low thermal conductivity including large, complex unit cells, high average atomic mass, high average atomic volume and structural, mass and bonding disorder. Promising materials might include Dion-Jacobsen phases such as $AB_2C_3O_{10}$ (A = rare earth, B = alkali rare earth and C = transition metal), layered cuprates, cobaltites $Sr_2(Y_{1-x}Ca_x)Co_2O_6$ [55], molybdates $CsBi(MoO_4)_2$, exfoliated tungstates (2-dimensional pyrochlore) $Cs_{(6+x)}W_{11}O_{36}$ [56], and intergrowth phases[57] $Bi_4LnNb_3O_{15}$ / $Bi_4LaTa_3O_{15}$ (Ln = La, Pr, Nd).

Additionally, solid-solutions of existing layered oxides may be constructive starting points for searching out new materials. For example, $Bi_{2-x}Sr_{2+x}Ti_{1-x}Nb_{2+x}O_{12}$ [58] is particularly appealing because the end members, $Bi_4Ti_3O_{12}$ and $Sr_2Nb_2O_7$, have nearly identical thermal conductivity and recent studies have shown that up to 30% solid-solubility exists in the series. Both Bi and Nb cations are over twice as massive as the atoms they substitute therefore, the increased mass disorder on both cation sites should further scatter phonons in the solid-solution region and result in a minimum value of thermal conductivity for the most disordered compound in the series, x=0 ($Bi_2Sr_2TiNb_2O_{12}$).

6. Conclusion

The thermal properties of polycrystalline samples of $RE_2SrAl_2O_7$ (RE = La, Nd, Sm, Eu, Gd, Dy) and highly textured and polycrystalline samples 0.5 mol% La doped $Sr_2Nb_2O_7$ have been measured from just above room temperature (35^{o}C) to 1000^{o}C. The thermal conductivity was found to be very low (~1 W/mK for strontium niobate and ~2.2 W/mK for rare-earth strontium aluminate) and in several cases temperature independent from 35^{o}C up to 1000^{o}C. The thermal conductivity of the rare-earth strontium aluminates is found to be strongly dependent on the individual rare-earth ion even though the rare-earths that can form the complex strontium aluminate structure can only vary over a very narrow range of atomic weight, from La^{3+} to Ho^{3+}. The lowest thermal conductivity of the series of compounds, that of

the dysprosium strontium aluminate, is comparable with that of yttria-stabilized zirconia despite the fact that the aluminates do not contain oxygen vacancies as the zirconia does. Additionally, the strontium niobate was found to be strongly anisotropic parallel and perpendicular to the layered structure over all temperatures measured. The phase transition in the strontium niobate compound between the room temperature normal orthorhombic phase and the incommensurate orthorhombic phase above 215^{o}C has a smaller than expected effect on thermal conductivity considering the significant structural modulation associated with the phase transition. In both layered oxide material systems it is tempting to attribute the low thermal conductivity, as well as the thermal anisotropy in the $Sr_2Nb_2O_7$ compound, to phonon scattering related to the density difference between blocks comprising the in the natural superlattice structure of layered oxides.

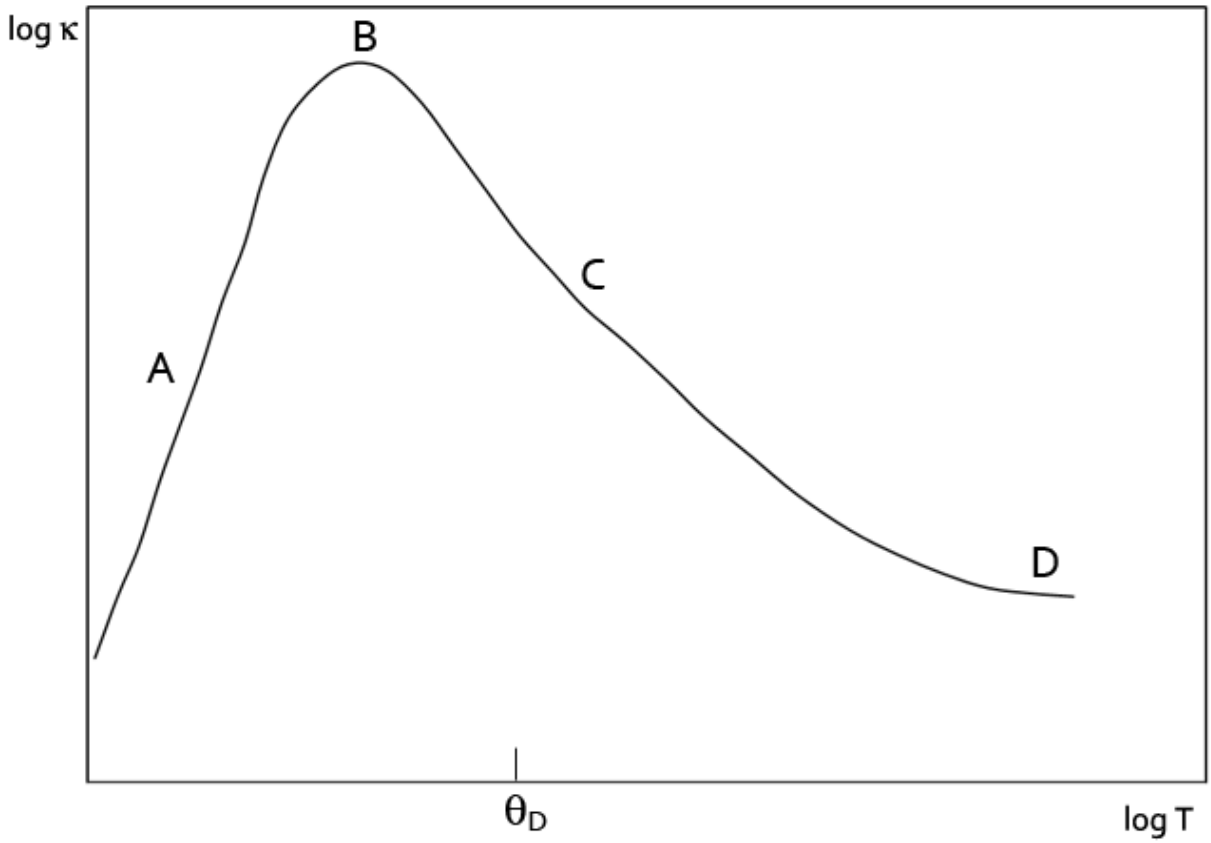

Figure 1. Logarithmic plot of thermal conductivity versus temperature for a non-metallic crystal. There are four characteristic regimes A, B, C and D corresponding to different phonon scattering processes.

Table 1.

Lattice parameter and site occupancy information for $RE_2SrAl_2O_7$ (RE = La, Nd, Sm, Eu, Gd, Dy)

Rare-Earth Ion	La	Nd	Sm	Eu	Gd	Dy
a	0.37712	0.3724	0.37159	0.37101	0.37052	0.37053
c	2.0197	1.9938	1.9876	1.9831	1.9781	1.9565
A1 RE^{3+} occupancy	.73	.54	.43	.32	.28	.21
A2 RE^{3+} occupancy	1.27	1.46	1.56	1.67	1.72	1.79
$\rho_{Rocksalt}/\rho_{Perovskite}$	0.938	1.12	1.20	1.26	1.36	1.46

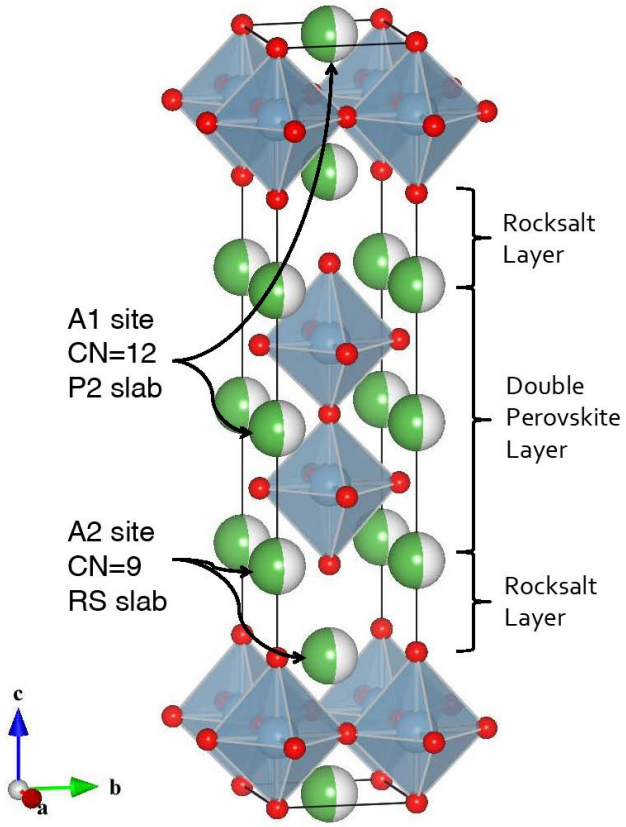

Figure 2. The tetragonal crystal structure of the n=2 member of the Ruddlesden-Popper phase structure of $RE_2SrAl_2O_7$. The green and white spheres represent A1 and A2 sites, the octahedra with small sphere vertices are AlO_6 octahedra. The A1 cation site is located in the perovskite layer and the A2 cation site is located in the rocksalt layer. Image produced using Vesta software[59].

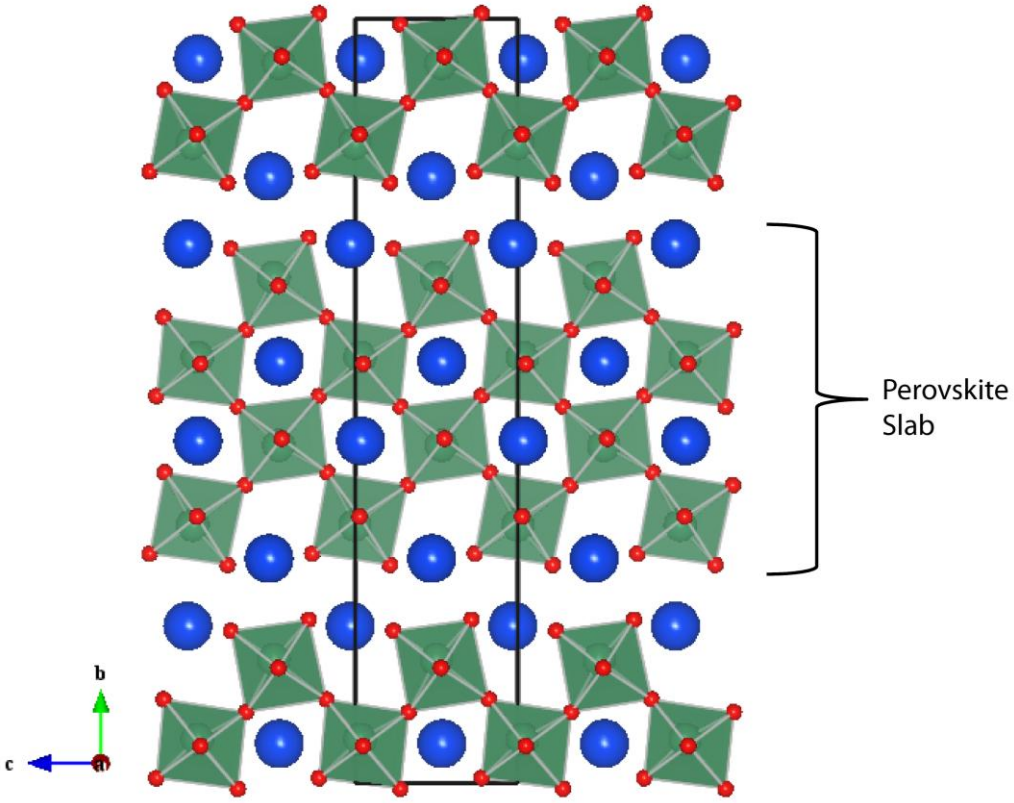

Figure 3. The orthorhombic crystal structure of the n=4 member of $Sr_nNb_nO_{3n+2}$ series viewed along the a-axis. The large spheres are Sr atoms and the octahedral with small sphere vertices are NbO_6 octahedra. Layers of perovskite like slabs are separated by additional planes of O atoms. The perovskite slabs are displaced by a/2 with respect to one another. The boxed area represents one unit cell. Image produced using VESTA software[59].

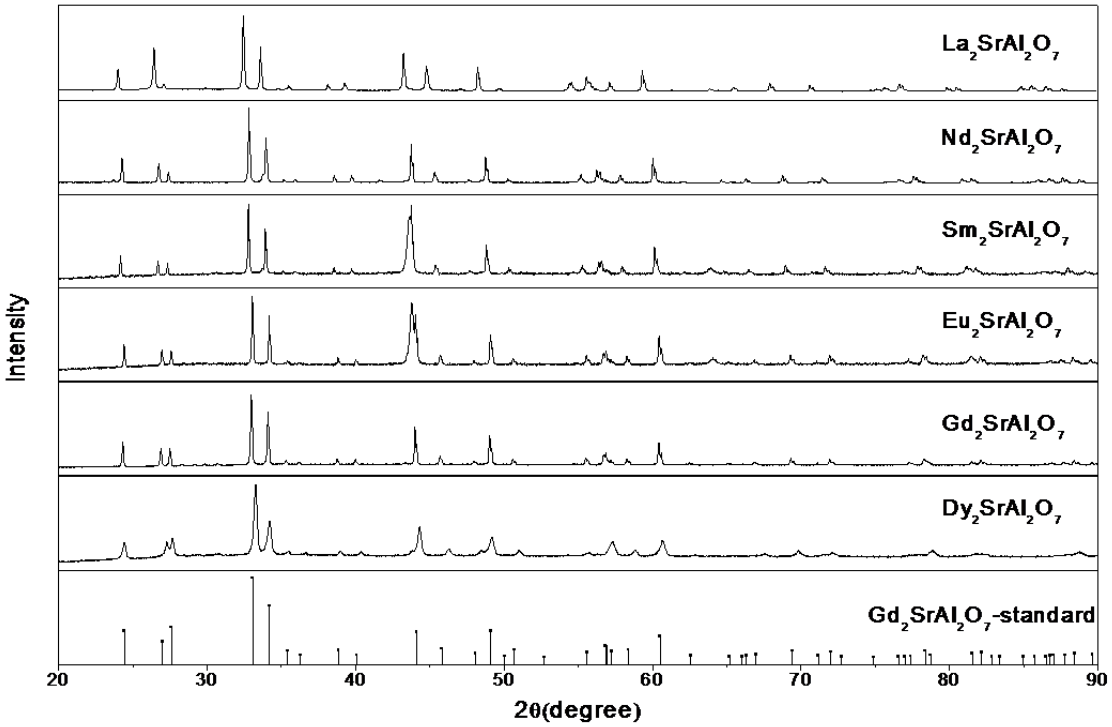

Figure 4. X-ray diffraction results for rare-earth strontium aluminates shown along with the $Gd_2SrAl_2O_7$ standard[60].

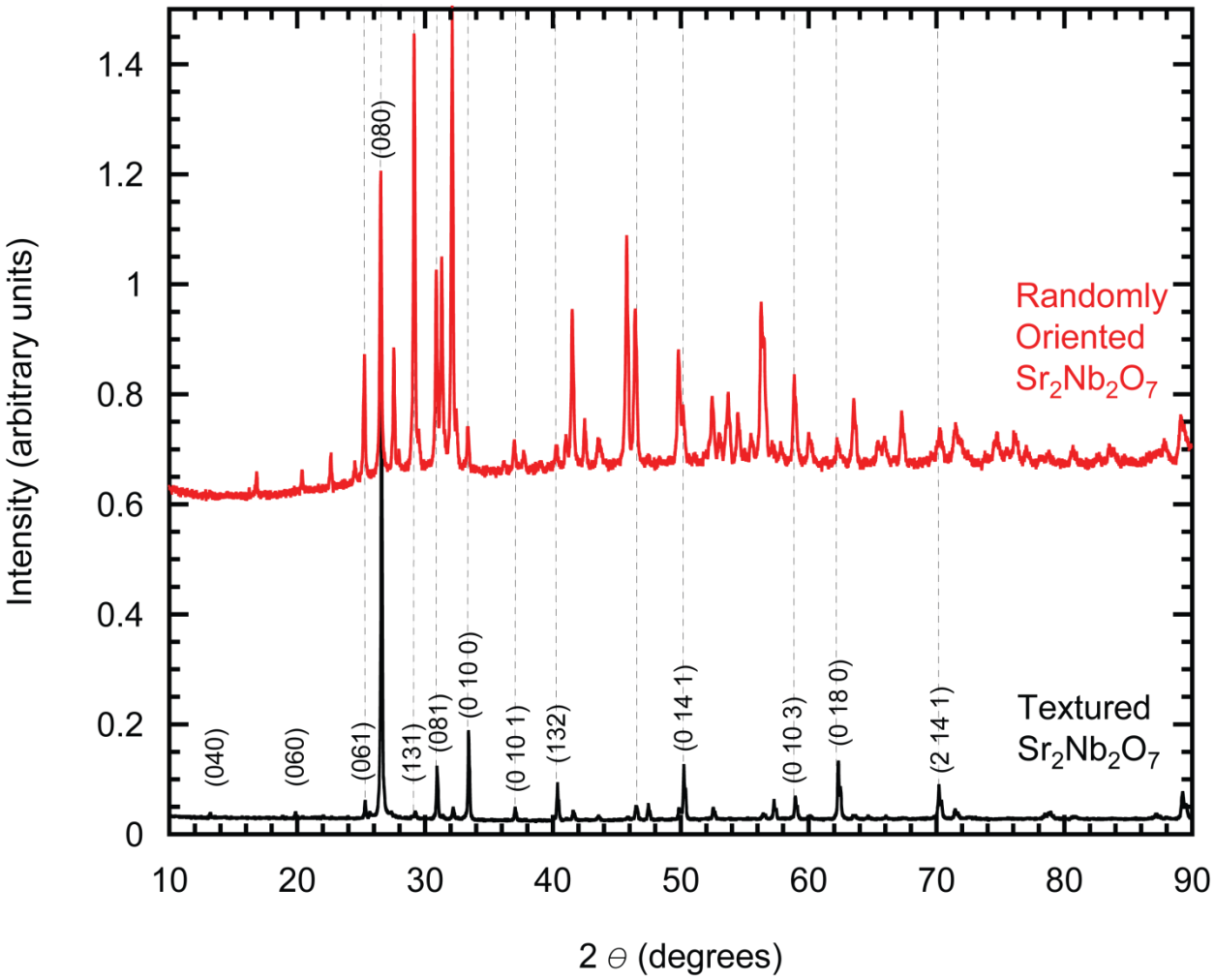

Figure 5. Normalized X-ray diffraction patterns from random (above) and textured (below) samples of $Sr_2Nb_2O_7$. Diffracted intensity from peaks corresponding to (0k0) dominate in the textured sample whereas the randomly oriented polycrystalline sample matches the expected peak pattern for $Sr_2Nb_2O_7$ orthorhombic unit cell.

Table 2.

Physical Properties

Composition	X-ray Density ($kg\ m^{-3}$)	Relative Density	Young's Modulus (GPa)	Unit Cell Volume (nm^3)
$La_2SrAl_2O_7$	6129	0.881	166.4	0.2872
$Nd_2SrAl_2O_7$	6479	0.990	186.0	0.2783
$Sm_2SrAl_2O_7$	6694	0.948	252.3	0.2744
$Eu_2SrAl_2O_7$	6762	0.980	240.0	0.2730
$Gd_2SrAl_2O_7$	6936	0.955	257.9	0.2716
$Dy_2SrAl_2O_7$	7173	0.962	230.4	0.2686
Textured La doped $Sr_2Nb_2O_7$	5316	0.978	c_{11} = 101.9* c_{22} = 139* c_{33} = 102.7*	0.5974
Polycrystalline La doped $Sr_2Nb_2O_7$	5316	0.991		0.5974

*Taken from Shabbir et al.[52]

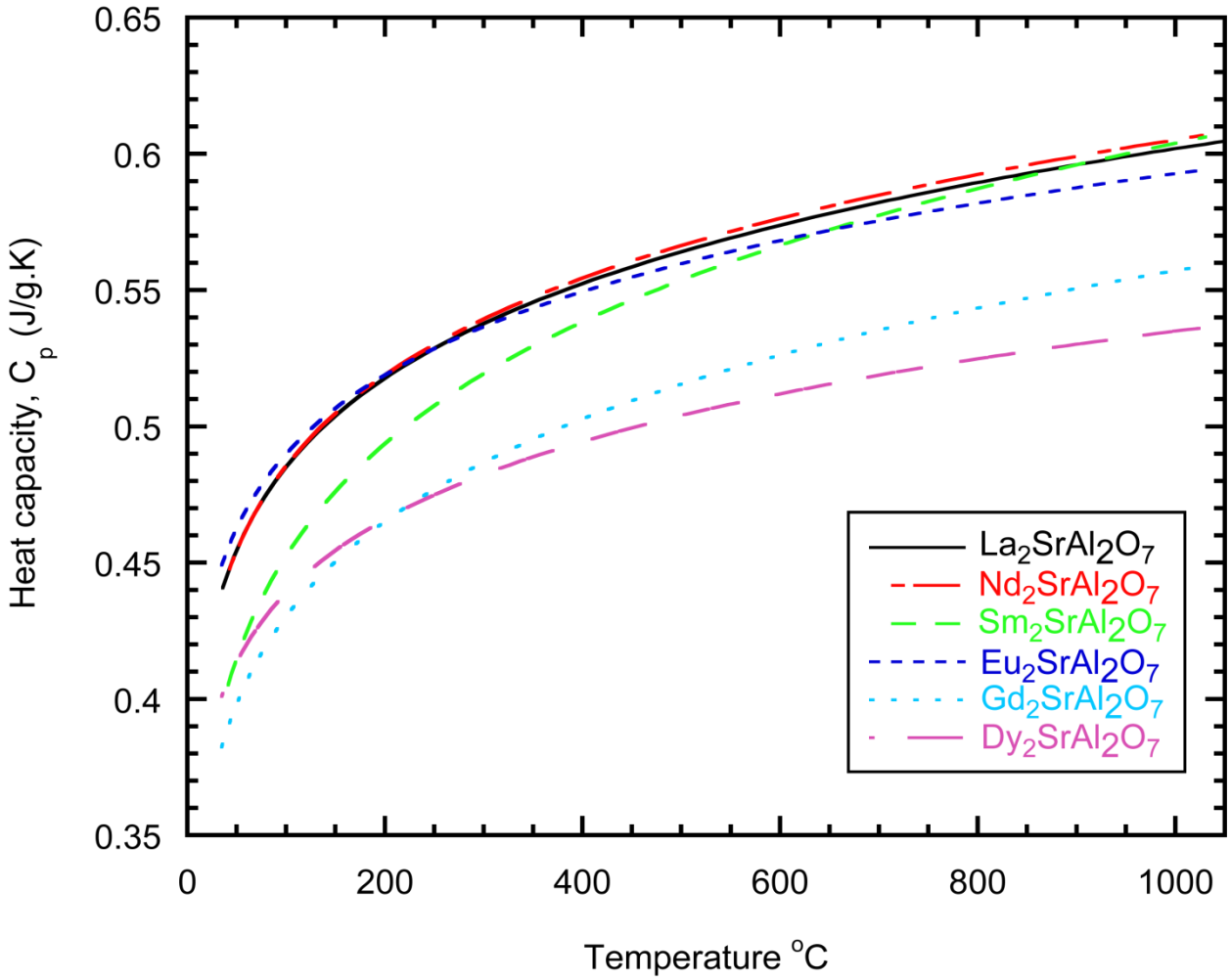

Figure 6. Heat capacity as a function of temperature for the rare-earth strontium aluminates. These values are within 4% of the calculated value using Neumann-Kopp rule.

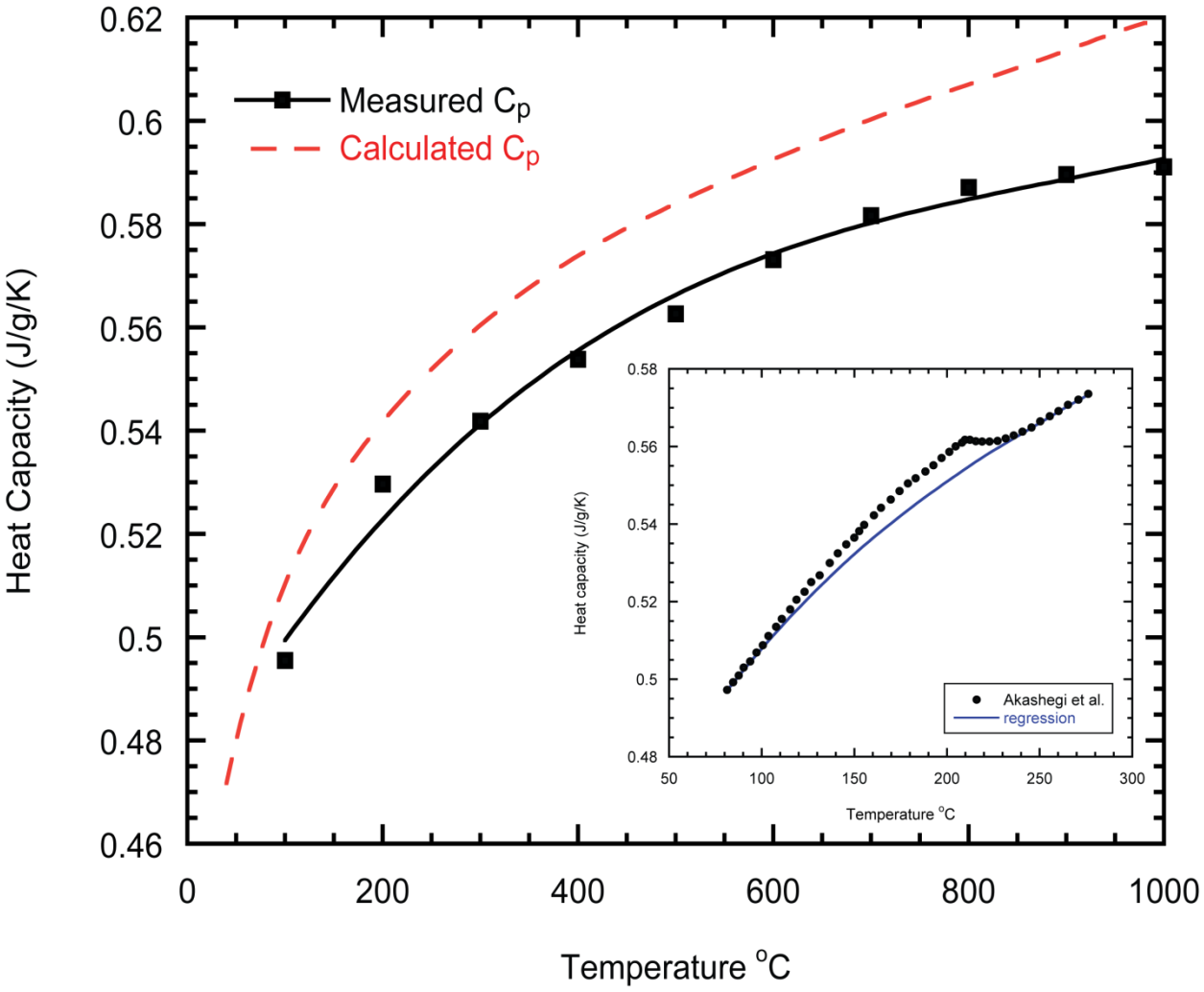

Figure 7. Heat capacity of textured $Sr_2Nb_2O_7$. Measurement results were compared to results calculated according to the Neumann-Kopp rule (dashed line) and shown to be within 4.2%. The solid line is a guide for the eye. The second order phase transition is shown inset along with the extrapolated baseline.

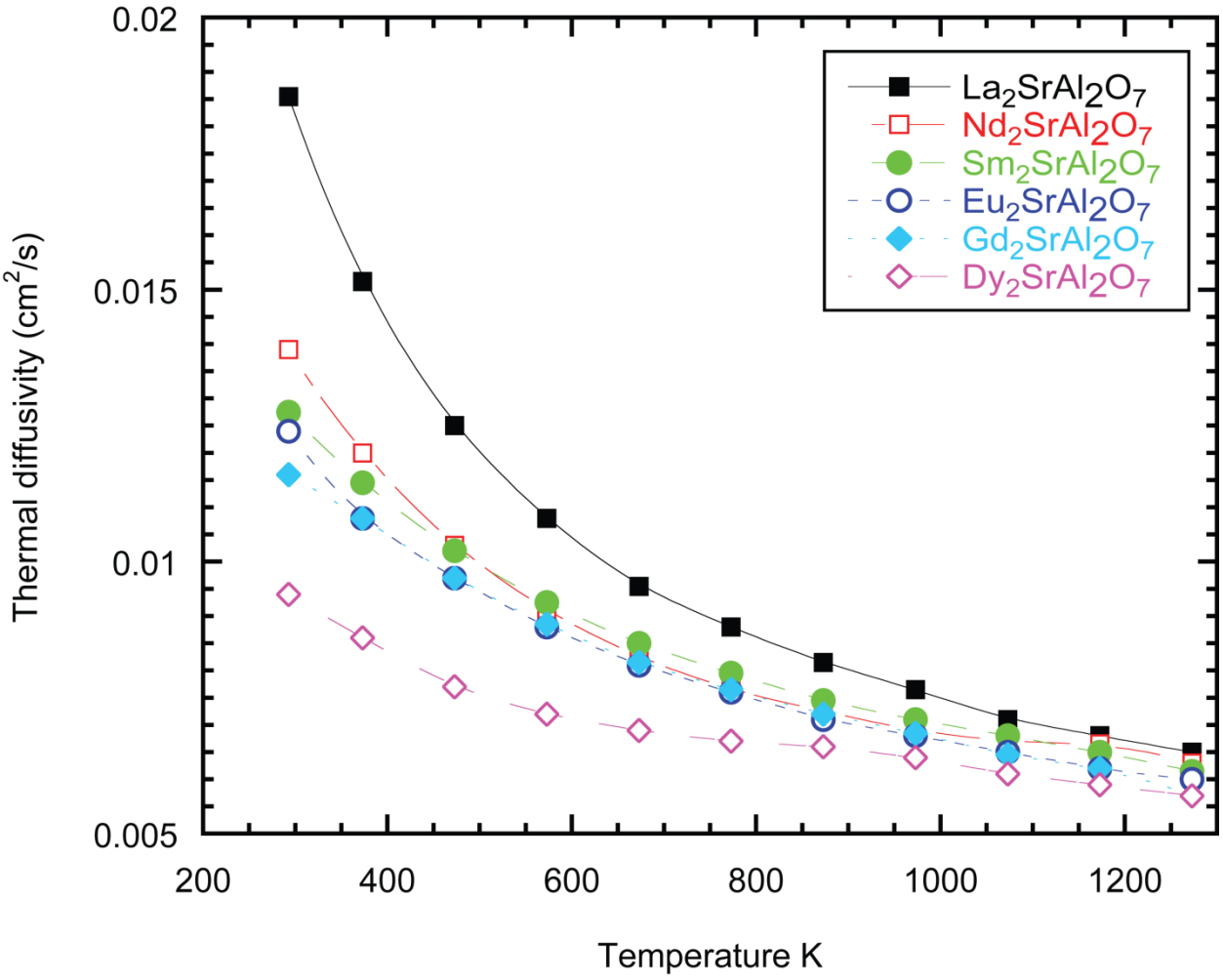

Figure 8. Thermal diffusivity of rare-earth strontium aluminates plotted against temperature.

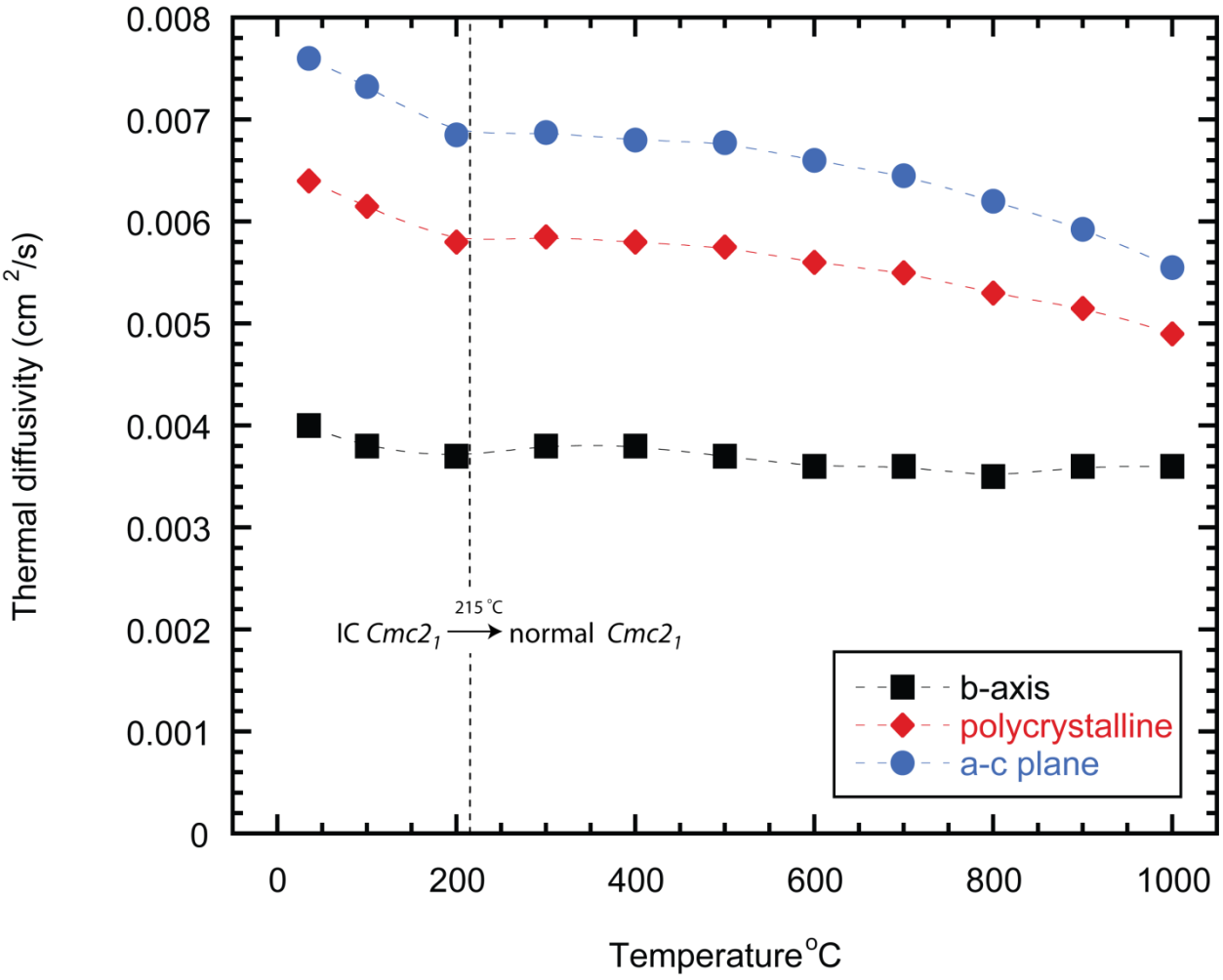

Figure 9. Thermal diffusivity as a function of temperature along the b-axis and randomly oriented material. The thermal conductivity along the layered planes (a-c plane), calculated from the other diffusivities, is also shown.

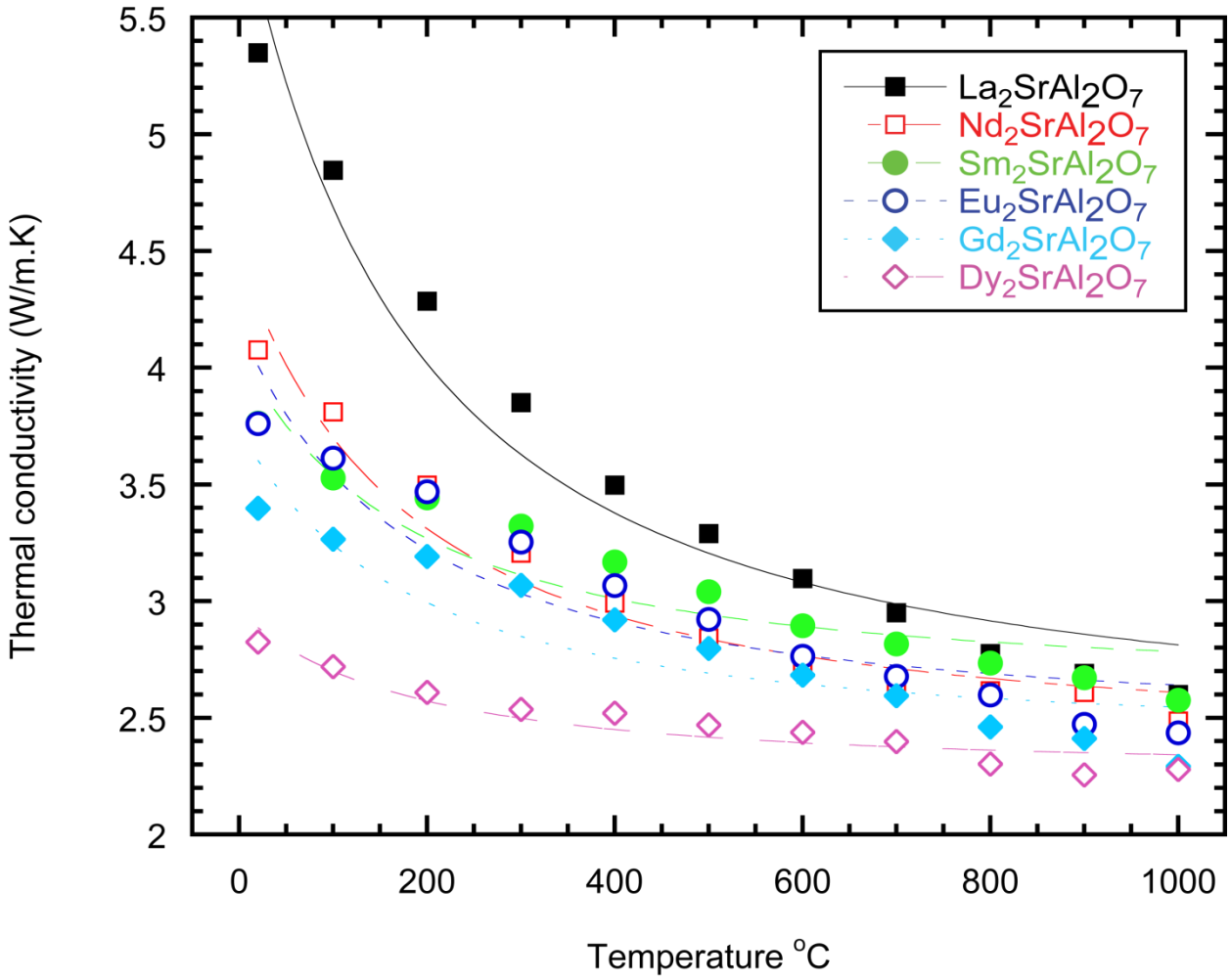

Figure 10. Thermal conductivity of rare-earth strontium aluminates as a function of temperature. The lines represent best fit regressions based on Mevrel's model.

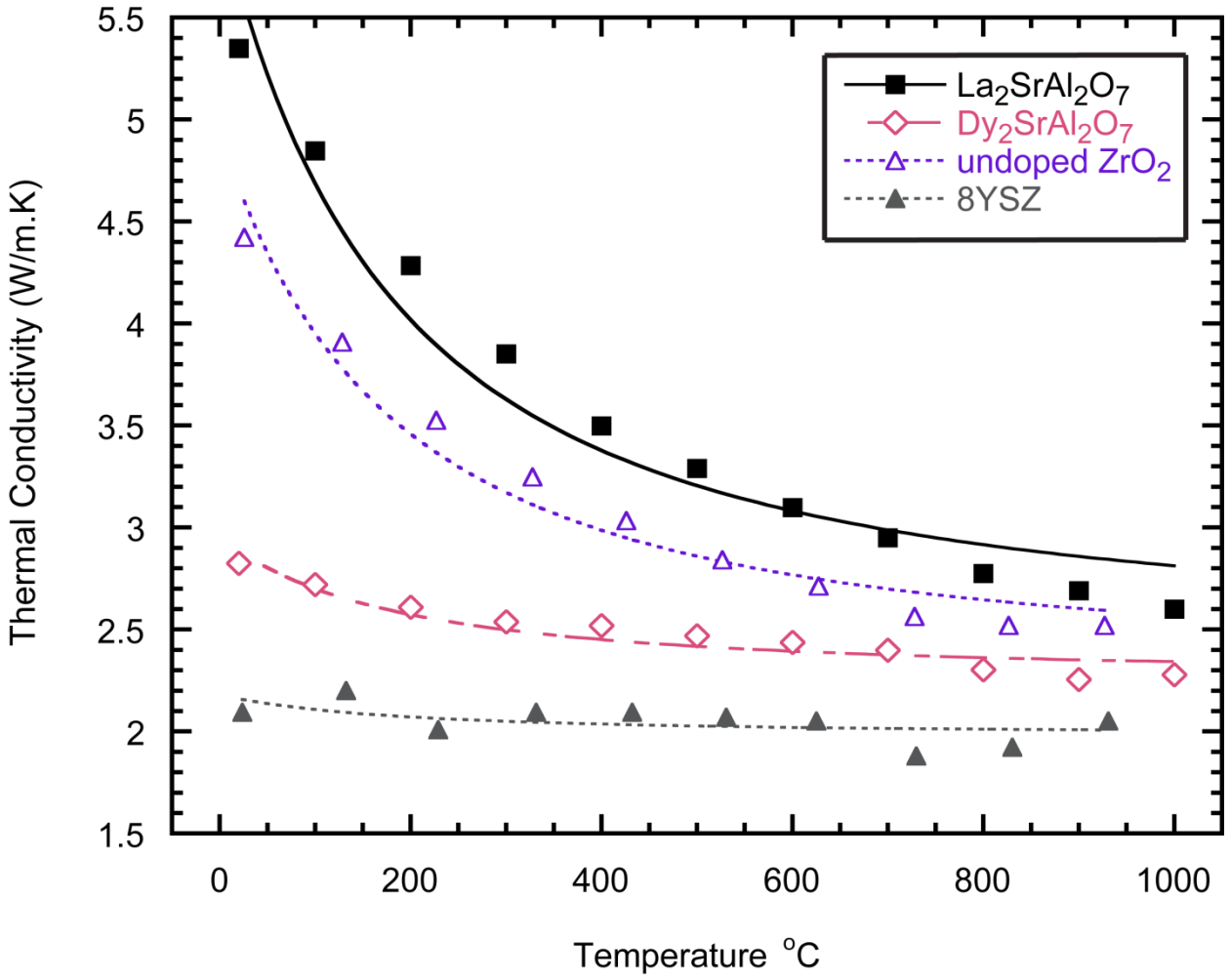

Figure 11. Thermal conductivity of end members of the $RE_2SrAl_2O_7$ series (RE = La, Dy) plotted along with undoped and 8 mol% yttria-stabilized zirconia for comparison.

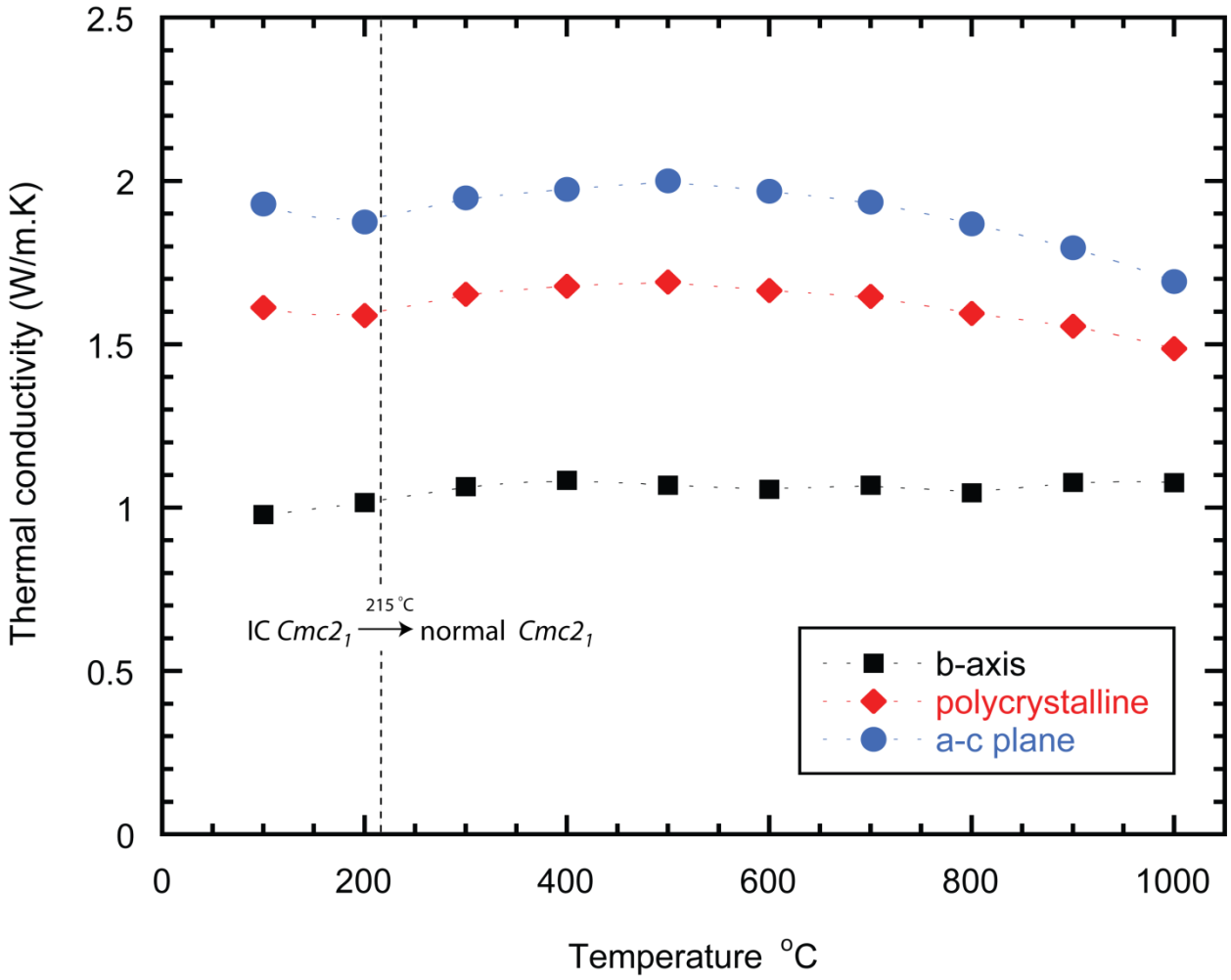

Figure 12. Thermal conductivity as a function of temperature along the b-axis of the textured materials and of the randomly oriented material. The calculated thermal conductivity along the layered planes (a-c plane) is also shown.

Table 3.

The fitting parameters for the $RE_2SrAl_2O_7$ (RE= La, Nd, Sm, Eu, Gd, Dy) series.

Rare-Earth Ion	La	Nd	Sm	Eu	Gd	Dy
A (W/m)	1623	1153	934	998	725	525
T_1 (K)	220	167	118	135	100	77
R^2	.958	.962	.851	.862	.648	.898
K_{min} (W/mK)	2.4595	2.3126	2.638	2.4702	2.4154	2.2748

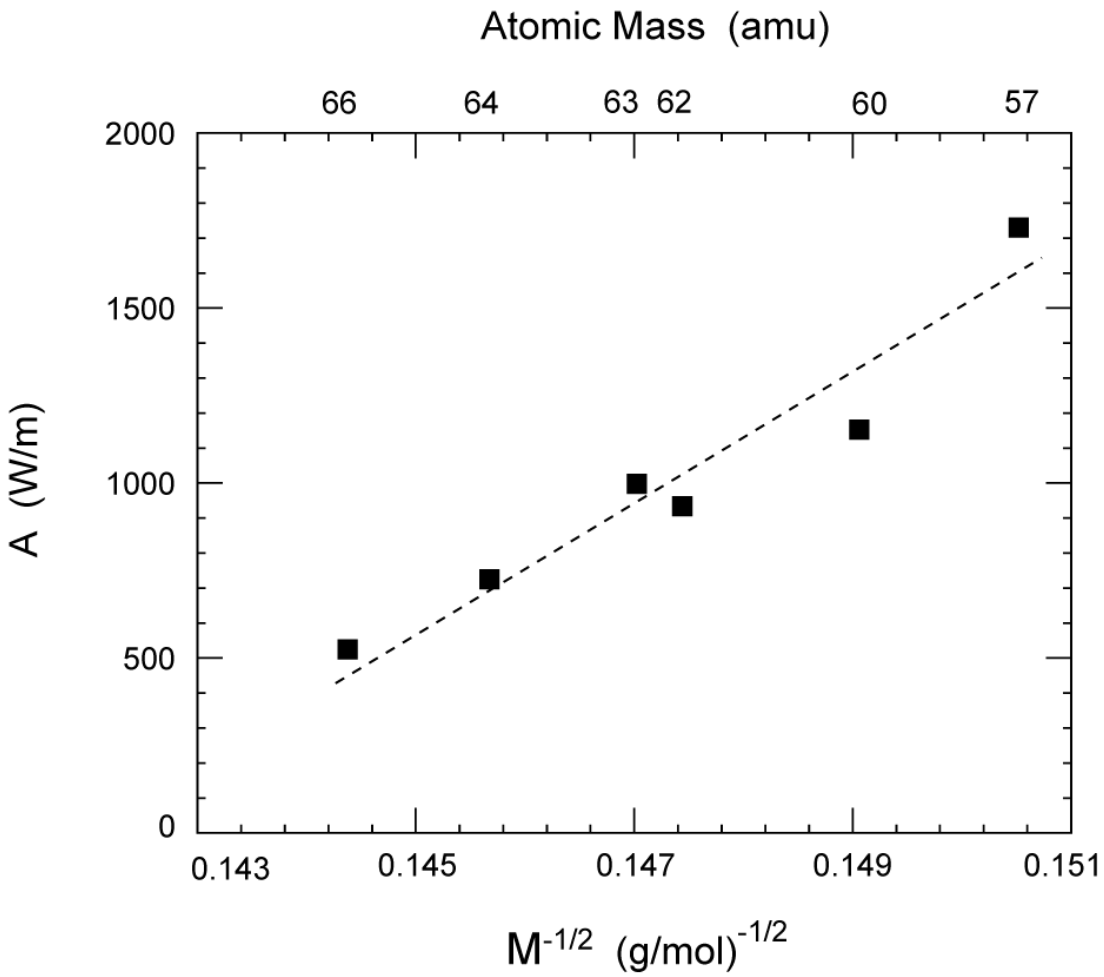

Figure 13. Linear dependence of fitting parameter A versus $M^{-1/2}$ agrees with prediction by Grimvall.

REFERENCES

[1]J. G. Bednorz and K. A. Müller, "Possible highTc superconductivity in the Ba−La−Cu−O system," *Zeitschrift für Physik B Condensed Matter,* **64**[2] 189 (1986).

[2]M. K. Wu, J. R. Ashburn, C. J. Torng, P. H. Hor, R. L. Meng, L. Gao, Z. J. Huang, Y. Q. Wang, andC. W. Chu, "Superconductivity at 93 K in a new mixed-phase Y-Ba-Cu-O compound system at ambient pressure," *Physical Review Letters,* **58**[9] 908 (1987).

[3]T. K. Takeuchi, T., Takami, T., Takahashi, H., Ikuta, H., Mizutani, U., Soda, K., Funahashi, R., Shikano, M., Mikami, M., Tsuda, S., Yokoya, T., Shin, S., Muro, T., "Contribution of electronic structure to the large thermoelectric power in layered cobalt oxides," *Physical Review B,* **69** 125410 (2004).

[4]I. Terasaki, Sasago, Y., Uchinokura, K., "Large thermoelectric power in NaCo2O4 single crystals," *Physical Review B,* **56** R12685-87 (1997).

[5]R. Mahesh, R. Mahendiran, A. K. Raychaudhuri, andC. N. R. Rao, "Effect of the Internal Pressure Due to the A-Site Cations on the Giant Magnetoresistance and Related Properties of Doped Rare Earth Manganates, Ln1-xAxMnO3 (Ln = La, Nd, Gd, Y; A = Ca, Sr, Ba, Pb)," *Journal of Solid State Chemistry,* **120**[1] 204 (1995).

[6]C. N. R. Rao, A. K. Cheetham, andR. Mahesh, "Giant Magnetoresistance and Related Properties of Rare-Earth Manganates and Other Oxide Systems," *Chemistry of Materials,* **8**[10] 2421-32 (1996).

[7]J. Bardeen, G. Rickayzen, andL. Tewordt, "Theory of the Thermal Conductivity of Superconductors," *Physical Review,* **113**[4] 982 (1959).

[8]S. Schmitt-Rink, K. Miyake, andC. M. Varma, "Transport and Thermal Properties of Heavy-Fermion Superconductors: A Unified Picture," *Physical Review Letters,* **57**[20] 2575 (1986).

[9]C. Uher, "Thermal conductivity of high-Tc superconductors," *Journal of Superconductivity,* **3**[4] 337 (1990).

[10]R. C. Yu, M. B. Salamon, J. P. Lu, andW. C. Lee, "Thermal conductivity of an untwinned YBa2Cu3O7- delta single crystal and a new interpretation of the superconducting state thermal transport," *Physical Review Letters,* **69**[9] 1431 (1992).

[11]G. Grimvall, "Thermophysical Properties of Materials." North-Holland Press: Amsterdam, (1986).

[12]C. Kittel, "Introduction to Solid State Physics." Wiley, (1995).

[13]J. Callaway and H. C. von Baeyer, "Effect of Point Imperfections on Lattice Thermal Conductivity," *Physical Review,* **120**[4] 1149 (1960).

[14]M. C. Roufosse and P. G. Klemens, "Lattice Thermal Conductivity of Minerals at High Temperatures," *Journal of Geophysical Research,* **79**[5] 703-05 (1974).

[15]R. Mévrel, J.-C. Laizet, A. Azzopardi, B. Leclercq, M. Poulain, O. Lavigne, andD. Demange, "Thermal diffusivity and conductivity of Zr1-xYxO2-x/2 (x=0, 0.084 and 0.179) single crystals," *Journal of the European Ceramic Society,* **24**[10-11] 3081 (2004).
[16]D. R. Clarke, "Materials selection guidelines for low thermal conductivity thermal barrier coatings," *Surface and Coatings Technology,* **163-164** 67 (2003).
[17]R. M. Costescu, Cahill, D. G., Fabreguette, F. H., Sechrist, Z. A., George, S. M., "Ultra-Low Thermal Conductivity in W/Al2O3 Nanolaminates," *Science,* **303**[5660] 989-90 (2004).
[18]C. Chiritescu, D. G. Cahill, N. Nguyen, D. Johnson, A. Bodapati, P. Keblinski, andP. Zschack, "Ultralow Thermal Conductivity in Disordered, Layered WSe2 Crystals," *Science* 1136494 (2006).
[19]M. Dion, Ganne, M., Tournoux, M., *Rev. Chim. Minerale,* **23** 61-69 (1986).
[20]M. Dion, Ganne, M., Tournoux, M., Ravez, J., *Rev. Chim. Minerale,* **21** 92-103 (1984).
[21]M. Dion, Ganne, M., Tournoux, M., "Probing Octahedral Tilting in Dion-Jacobson Layered Perovskites With Neutron Powder Diffraction and Raman Spectroscopy," *Materials Research Bulletin,* **16** 1429-35 (1981).
[22]B. Aurivillius, "Mixed bismuth oxides with layer lattices: II. Structure of Bi4Ti3O12," *Arkiv for Kemi,* **1**[58] 499-512 (1949).
[23]Y. Shen, Clarke, D. R., Fuierer, P. A., "Anisotropic thermal conductivity of the Aurivillus phase, bismuth titanate (Bi4Ti3O12): A natural nanostructured superlattice," *Applied Physics Letters,* **93**[10] 102907 (2008).
[24]S. N. Ruddlesden and P. Popper, "On the crystal structure of the nitrides of silicon and germanium," *Acta Crystallographica,* **11**[7] 465-68 (1958).
[25]S. N. Ruddlesden and P. Popper, "New compounds of the K2NIF4 type," *Acta Crystallographica,* **10**[8] 538-39 (1957).
[26]C. Wan, Sparks, Taylor D., Clarke, David R., Pan, Wei, "Thermal Conductivity of Rare-earth Strontium Aluminates," (in press).
[27]T. D. Sparks, Fuierer, Paul A., Clarke, David R., "Anisotropic Thermal Diffusivity and Conductivity of La-doped Strontium Niobate Sr2Nb2O7," (in press).
[28]I. Zvereva, Y. Smirnov, V. Gusarov, V. Popova, andJ. Choisnet, "Complex aluminates RE2SrAl2O7 (RE = La, Nd, Sm-Ho): Cation ordering and stability of the double perovskite slab-rocksalt layer P2/RS intergrowth," *Solid State Sciences,* **5**[2] 343 (2003).
[29]S. C. Abrahams, Schmalle, H. W., Williams, T., Williams, Reller, A., Lichtenberg, F., Widmer, D., Bednorz, J. G., Spreiter, R., Bosshard, Ch., Günter, P., "Centrosymmetric or Noncentrosymmetric? Case Study, Generalization and Structural Redetermination of Sr5Nb5O17," *Acta Crystallographica,* **B54** 399-416 (1998).

[30]L. Elcoro, J. M. Perez-Mato, andR. L. Withers, "Intergrowth polytypoids as modulated structures: a superspace description of the Srn(Nb,Ti)nO3n + 2 compound series," *Acta Crystallographica Section B,* **57**[4] 471-84 (2001).
[31]N. Ishizawa, F. Marumo, T. Kawamura, andM. Kimura, "The crystal structure of Sr2Nb2O7, a compound with perovskite-type slabs," *Acta Crystallographica Section B,* **31**[7] 1912-15 (1975).
[32]H. W. Schmalle, T. Williams, A. Reller, F. Lichtenberg, D. Widmer, andJ. G. Bednorz, "A Novel Semiconducting Perovskite-Related Phase: Sr5Nb5O17," *Acta Crystallographica Section C,* **51**[7] 1243-46 (1995).
[33]T. Williams, Lichtenberg, F., Widmer, D., Bednorz, J. G., Reller, A., "Layered Perovskitic Structures in Pure and Doped LaTiO3.5-x and SrNbO3.5-x," *Journal of Solid State Chemistry,* **103**[2] 375-86 (1993).
[34]F. Lichtenberg, Herrnberger, A., Wiedenmann, K. & Mannhart, J., *Progress in Solid State Chemistry,* **29** 1-70 (2001).
[35]K. Ohi, Kojima, S., "Successive Phase Transitions and Their Soft Modes in Ferroelectric Sr2Nb2O7," *Japanese Journal of Applied Physics,* **24**[24-2] 817-19 (1985).
[36]N. Yamamoto, "High-resolution electron microscopy of the incommensurate structure in Sr2Nb2O2," *Acta Crystallographica Section A,* **38**[6] 780-89 (1982).
[37]N. Yamamoto, Yagi, K., Honjo, G., Kimura, M., Kawamura, T., "New Phases of Sr2Ta2O7 and Sr2Nb2O7 Found by Electron Microscopy and Diffraction," *Journal of the Physical Society of Japan,* **48** 185-91 (1980).
[38]B. Brahmaroutu, G. L. Messing, andS. Trolier-McKinstry, "Densification and anisotropic grain growth in Sr2Nb2O7," *Journal of Materials Science,* **35**[22] 5673 (2000).
[39]R. E. N. Paul A. Fuierer, "La2Ti2O7 Ceramics," *Journal of the American Ceramic Society,* **74**[11] 2876-81 (1991).
[40]L. M. Clark III and R. E. Taylor, "Radiation loss in the flash method for thermal diffusivity," *Journal of Applied Physics,* **46**[2] 714 (1975).
[41]L. Chen and D. R. Clarke, "A numerical solution based parameter estimation method for flash thermal diffusivity measurements," *Computational Materials Science,* **45**[2] 342 (2009).
[42]"International Center for Diffraction Data File 01-070-0114." in**.**
[43]F. K. Lotgering, *Journal of Inorganic and Nuclear Chemistry,* **9** 113 (1959).
[44]I. Barin, "Thermochemical Data of Pure Substances," 2 ed. VCH: Weinheim, (1993).
[45]D. R. Clarke and S. R. Phillpot, "Thermal barrier coating materials," *Materials Today,* **8**[6] 22 (2005).
[46]P. G. Klemens, "Thermal Resistance due to Point Defects at High Temperatures," *Physical Review,* **119**[2] 507 (1960).

[47]P. G. Klemens, "Phonon scattering by oxygen vacancies in ceramics," *Physica B: Condensed Matter,* **263-264** 102 (1999).
[48]M. R. Winter, Clarke, David R., "Oxide Materials with Low Thermal Conductivity," *Journal of the American Ceramic Society,* **90**[2] 533-40 (2007).
[49]B. Abeles, "Lattice Thermal Conductivity of Disordered Semiconductor Alloys at High Temperatures," *Physical Review,* **131**[5] 1906 (1963).
[50]M. R. Winter and D. R. Clarke, "Thermal conductivity of yttria-stabilized zirconia-hafnia solid solutions," *Acta Materialia,* **54**[19] 5051 (2006).
[51]J. F. Nye, " Physical Properties of Crystals. Their Representation by Tensors and Matrices.″ Oxford Science Publications.: Oxford, UK, (1985).
[52]G. Shabbir and S. Kojima, "Acoustic and thermal properties of strontium pyroniobate single crystals," *Journal of Physics D: Applied Physics*[8] 1036 (2003).
[53]V. Lughi, Clarke, D. R., "Transformation of Electron-Beam Physical Vapor-Deposited 8 wt% Yttria-Stabilized Zirconia Thermal Barrier Coatings," *Journal of the American Ceramic Society,* **88**[9] 2552-58 (2005).
[54]P. G. Klemens, "Theory of Thermal Conductivity in Solids,″ pp. 1-68. Academic Press: New York, (1969).
[55]K. Yamaura, Q. Huang, R. W. Erwin, J. W. Lynn, and R. J. Cava, "Anomalous crystal-structure distortion at the antiferromagnetic transition in the layered cobalt oxide Sr2Y0.8Ca0.2Co2O6," *Physical Review B,* **60**[13] 9623 (1999).
[56]K. Fukuda, K. Akatsuka, Y. Ebina, R. Ma, K. Takada, I. Nakai, and T. Sasaki, "Exfoliated nanosheet crystallite of cesium tungstate with 2D pyrochlore structure: synthesis, characterization, and photochromic properties.," *ACS Nano,* **2**[8] 1689-95 (2008).
[57]T. K. Mandal, S. Augustine, J. Gopalakrishnan, and P. Boullay, "Bi4LnNb3O15 (Ln = La, Pr, Nd) and Bi4LaTa3O15: New intergrowth Aurivillius related phases," *Materials Research Bulletin,* **40**[6] 920 (2005).
[58]C. H. Hervoches and P. Lightfoot, "Cation Disorder in Three-Layer Aurivillius Phases: Structural Studies of Bi2-xSr2+xTi1-xNb2+xO12 (0<x<0.8) and Bi4-xLaxTi3O12 (x=1 and 2)," *Journal of Solid State Chemistry,* **153**[1] 66 (2000).
[59]K. Momma, Izumi, F., "VESTA: a three-dimensional visualization system for electronic and structural analysis," *Journal of Applied Crystallography,* **41** 653-58 (2008).
[60]"International Center for Diffraction Data File 01-076-0095."